FisB relies on homo-oligomerization and lipid-binding to catalyze membrane fission in bacteria

Ane Landajuela[1,2†*], Martha Braun[2,3†], Christopher D. A. Rodrigues[4], Alejandro Martínez-Calvo[5], Thierry Doan[6], Florian Horenkamp[7#], Anna Andronicos[1‡], Vladimir Shteyn[1,2,] Nathan D. Williams[2,7], Chenxiang Lin[2,7], Ned S. Wingreen[8,9], David Z. Rudner[10], Erdem Karatekin[1,2,3,11*]

1 Cellular and Molecular Physiology, Yale University, New Haven, CT, USA

2 Nanobiology Institute, Yale University, West Haven, CT, USA

3 Molecular Biophysics and Biochemistry, Yale University, New Haven, CT, USA

4 iThree Institute, University of Technology Sydney (UTS), Australia

5 Grupo de Mecánica de Fluidos, Universidad Carlos III de Madrid, Spain

6 Laboratoire d'Ingénierie des Systèmes Macromoléculaires, Aix-Marseille Université - CNRS UMR7255, Marseilles, France

7 Cell Biology, Yale University

8 Department of Molecular Biology, Princeton University, Princeton, NJ 08544, USA.

9 Lewis-Sigler Institute for Integrative Genomics, Princeton University, Princeton, NJ 08544, USA.

10 Department of Microbiology, Harvard Medical School, Boston MA

11 Université de Paris, SPPIN - Saints-Pères Paris Institute for the Neurosciences, Centre National de la Recherche Scientifique (CNRS), F-75006 Paris, France.

† These authors contributed equally

Present address: Pfizer, New London, CT

‡ Present address: Department of Biological Chemistry, School of Medicine, U. California Irvine

* To whom correspondence should be addressed

ane.landajuela@yale.edu

erdem.karatekin@yale.edu (lead contact)

ABSTRACT

Little is known about mechanisms of membrane fission in bacteria despite their requirement for cytokinesis. The only known dedicated membrane fission machinery in bacteria, FisB, is expressed during sporulation in *Bacillus subtilis* and is required to release the developing spore into the mother cell cytoplasm. Here we characterized the requirements for FisB-mediated membrane fission. FisB forms mobile clusters of ~12 molecules that give way to an immobile cluster at the engulfment pole containing ~40 proteins at the time of membrane fission. Analysis of FisB mutants revealed that binding to acidic lipids and homo-oligomerization are both critical for targeting FisB to the engulfment pole and membrane fission. Experiments using artificial membranes and filamentous cells suggest FisB does not have an intrinsic ability to sense or induce membrane curvature but can bridge membranes. Finally, modeling suggests homo-oligomerization and trans interactions with membranes are sufficient to explain FisB accumulation at the membrane neck that connects the engulfment membrane to the rest of the mother cell membrane during late stages of engulfment. Together, our results show that FisB is a robust and unusual membrane fission protein that relies on homo-oligomerization, lipid-binding and the unique membrane topology generated during engulfment for localization and membrane scission, but surprisingly, not on lipid microdomains, negative-curvature lipids, or curvature-sensing.

INTRODUCTION

Membrane fission is a fundamental process required for endocytosis[1], membrane trafficking[2], enveloped virus budding[3], phagocytosis[4], cell division[5] and sporulation[6-8]. During membrane fission, an initially continuous membrane divides into two separate ones. This process requires dynamic localization of specialized proteins, which generate the work required to merge membranes[9-13]. Dynamin[14] and the endosomal sorting complex required for transport III (ESCRT-III) catalyze many eukaryotic membrane fission reactions[15]. Both fission machineries bind acidic lipids, assemble into oligomers, and use hydrolysis of a nucleoside triphosphate (GTP or ATP) to achieve membrane fission. However, membrane fission can also be achieved by friction[16], stress accumulated at a boundary between lipid domains[17], forces generated by the acto-myosin network[18-21] or protein crowding[22]. By contrast, very little is known about membrane fission in bacteria, even though they rely on membrane fission for every division cycle.

We previously found that fission protein B (FisB) is required for the final membrane fission event during sporulation in *B. subtilis*[23]. When nutrients are scarce, bacteria in the orders *Bacillales* and *Clostridiales* initiate a developmental program that results in the production of highly resistant endospores[24]. Sporulation starts with an asymmetric cell division that generates a larger mother cell and a smaller forespore (Figure 1A). The mother cell membranes then engulf the forespore in a process similar to phagocytosis. At the end of engulfment, the leading membrane edge forms a small pore. Fission of this membrane neck connecting the engulfment membrane to the rest of the mother cell membrane releases the forespore, now surrounded by two membranes, into the mother cell cytoplasm (Figure 1A,B). At this late stage the mother nurtures the forespore as it prepares for dormancy. Once mature, the mother cell releases the spore into the environment through lysis. Spores can withstand heat, radiation, drought, antibiotics, and other environmental assaults for many years[25-28]. Under favorable conditions, the spore will germinate and restart the vegetative life cycle.

Conserved among endospore-forming bacteria, FisB is a mother-cell transmembrane protein expressed under the control of the transcription factor, σ^E, after asymmetric division[29]. In sporulating cells lacking FisB, engulfment proceeds normally but the final membrane fission event, detected using a lipophilic dye, is impaired[23] (Figure 1C,F and S1 Appendix Fig. 1A). During engulfment, FisB fused to a fluorescent protein forms dim, mobile clusters in the engulfment membrane (Figure 1D,E, Movie 1). When the engulfing membranes reach the cell pole, approximately 3 hours (t = 3h) after the onset of sporulation, a cluster of FisB molecules accumulates at the pole forming a more intense, immobile focus, where and when fission occurs (Figure 1D,E, Movie 2).

We had previously reported[23] that FisB interacts with cardiolipin (CL), a lipid enriched at cell poles[30-32] whose levels increase during sporulation[33] and is implicated in membrane fusion[34-36] and fission reactions[37]. In addition, CL was reported to act as a landmark for the polar recruitment of the proline transporter ProP, and the mechanosensitive channel MscSm[38,39]. Thus, it seemed plausible that CL could act as a landmark to recruit FisB to the membrane fission site and facilitate membrane fission. Apart from this hypothesis, no information has been available about how FisB localizes to the membrane fission site and how it may drive membrane scission.

97 Here, we determined the requirements for FisB's sub-cellular localization and
98 membrane fission during sporulation. Using quantitative analysis, we find small clusters
99 of ~12 FisB molecules diffuse around the mother cell membrane and ~40 copies of FisB
100 accumulate at the fission site as an immobile cluster to mediate membrane fission.
101 When FisB expression was lowered, ~6 copies of FisB were sufficient to drive
102 membrane fission, but fission took longer. Unexpectedly, FisB dynamics and membrane
103 fission are independent of both CL and phosphatidylethanolamine (PE), another lipid
104 implicated in membrane fusion and fission. We found FisB binds phosphatidylglycerol
105 (PG) with comparable affinity as CL, after adjusting for charge density. Thus, we
106 suspect that, as a more abundant lipid in the cell, PG can substitute for CL to bind FisB.
107 We tested other factors that may be important for the sub-cellular localization of FisB
108 and membrane fission. We found FisB dynamics are independent of flotillins, which
109 organize bacterial membranes into functional membrane microdomains[40], cell wall
110 synthesis machinery, and proton or voltage gradients across the membrane. Using
111 mutagenesis, we show that both FisB oligomerization and binding to acidic lipids are
112 required for proper localization and membrane fission. *B. subtilis ΔfisB* cells were
113 partially complemented by *C. perfringens* FisB, despite only ~23% identity between the
114 two proteins, suggesting a common localization and membrane fission mechanism
115 based on a few conserved biophysical properties. The membrane neck that eventually
116 undergoes fission and where FisB accumulates is the most highly curved membrane
117 region in the late stages of engulfment. Thus, FisB could potentially localize at the
118 membrane neck due to a preference for highly curved membrane regions. We tested
119 this possibility in experiments with both artificial giant unilamellar vesicles (GUVs) and
120 live cells. Surprisingly, these experiments failed to reveal any intrinsic affinity of FisB for
121 highly curved membranes. However, we found that FisB bridges membranes and
122 accumulates at membrane adhesion sites. Using modeling, we found that self-
123 oligomerization of FisB, coupled with its ability to bridge negatively charged membranes
124 is sufficient to explain its localization to the membrane neck. Thus, proteins can localize
125 to highly curved membrane regions through mechanisms independent of intrinsic
126 curvature sensitivity. Together, these results suggest FisB-FisB and FisB-lipid
127 interactions, combined with the unique membrane topology generated at the engulfment
128 pole during sporulation, provide a simple mechanism to recruit FisB to mediate
129 membrane fission independent of other factors.

130

131 **RESULTS**

132 **Membrane fission occurs in the presence of a cluster of FisB molecules**

133 To correlate FisB dynamics with membrane fission, we devised a labeling strategy that
134 allowed us to monitor both simultaneously, using a modified version of a fission assay
135 developed previously[41]. In this assay, synchronous sporulation is induced by placing *B.*
136 *subtilis* cells in a nutrient-poor medium. At different time points after the nutrient
137 downshift, aliquots are harvested from the culture, stained with the lipophilic membrane
138 dye FM4-64, mounted on an agar pad, and imaged using fluorescence microscopy. The
139 dye is virtually non-fluorescent in the medium, and it cannot cross the cell membrane.
140 Thus, before fission, FM4-64 labels the outer leaflet of both the mother cell and the
141 forespore membranes. After fission, only the outer leaflet of the mother cell is labeled

142 (S1 Appendix Figure 1B). Because post-fission cells and cells that never entered
143 sporulation are labeled identically, in addition to FM4-64, a fluorescent protein is
144 expressed in the forespore under the control of the forespore-specific transcription
145 factor σ^F to distinguish between the two cell types[42] (S1 Appendix Figure 1B). This
146 makes it challenging to monitor FisB dynamics simultaneously, which requires a third
147 channel. As an alternative, we used another lipophilic dye, TMA-DPH, that has partial
148 access to internal membranes but can distinguish between pre- and post-fission stages
149 without need for a forespore reporter[23] (Figure 1C and S1 Appendix Fig. 1D-G). Using
150 TMA-DPH as the fission reporter, we quantified the percentage of cells that have
151 undergone fission as a function of time, for wild-type, *fisB* knock-out (*ΔfisB*, strain
152 BDR1083, see S1 Appendix Table 2 for strains used), and *ΔfisB* cells complemented
153 with FisB fused to monomeric EGFP (mGFP-FisB, strain BAM003) as shown in Figure
154 1D and 1F. These kinetic measurements reproduced results obtained using FM4-64 (S1
155 Appendix Figure 1C). Thus, TMA-DPH can be used as a faithful reporter of membrane
156 fission, leaving a second channel for monitoring dynamics of FisB fused to a fluorescent
157 reporter.

158 In the experiments of Figure 1D and 1F, we simultaneously monitored dynamics of
159 mGFP-FisB and membrane fission. We found that membrane fission is almost always
160 accompanied by an intense, immobile mGFP-FisB signal at the engulfment pole (Figure
161 1D, time= 3hr into sporulation). This intense spot at the engulfment pole (ISEP) is
162 distinct from the dimmer, mobile clusters (DMC) that appear at earlier times elsewhere
163 (Figure 1D). By 3 h into sporulation, around 70 % of the cells expressing mGFP-FisB at
164 native levels had an ISEP (Figure 1G), a number that was close to the percentage of
165 cells that had undergone fission by then (Figure 1F). Scoring individual cells, we found
166 >90% (212/235) of cells that had undergone membrane fission also had an ISEP.

167 We also monitored membrane fission and mGFP-FisB signals in a strain with lower FisB
168 expression. Here, lower FisB expression is achieved by reducing the spacing between
169 the ribosome binding site (RBS) and the ATG start codon[43]. In this strain (BAL003),
170 there was an initial delay in the fraction of cells that had undergone fission, but fission
171 accelerated after t=3 h to reach near wild-type levels at around t=4h (Figure 1E,F). The
172 fraction of cells with an ISEP followed a similar pattern (Figure 1G). The fraction of cells
173 that had undergone fission at a given time was strongly correlated with the fraction of
174 cells with an ISEP at that time (Figure 1H). Scoring individual cells, we found >93%
175 (258/277) of cells that had undergone membrane fission had an ISEP. We conclude that
176 membrane fission occurs in the presence of a large immobile cluster of FisB molecules
177 at the site of fission.

178

179 **About 40 FisB molecules accumulate at the engulfment pole to mediate**
180 **membrane fission**

181 We asked how many copies of FisB are recruited to the engulfment pole at the time of
182 membrane fission and how this number is affected by the expression level. For this
183 quantification, we used DNA-origami based fluorescence standards we recently
184 developed[44]. These standards consist of DNA rods (~410 nm long and 7 nm wide)
185 labeled with AF647 at both ends and a controlled number of mEGFP molecules along

186 the rod (Figure 2A).

187 DNA-origami standards carrying different mEGFP copies were imaged using widefield
188 fluorescence microscopy (Figure 2B). For each type of rod, the average total
189 fluorescence intensity of single-rods was computed and plotted against the number of
190 mEGFP molecules per rod, generating the calibration curve in Figure 2D. We generated
191 *B. subtilis* cells expressing mEGFP-FisB at native levels (BAL001) in a *ΔfisB*
192 background so that images of these cells obtained under identical imaging conditions as
193 for the calibration curve in Figure 2D could be used to compute mEGFP-FisB copy
194 numbers. We imaged mEGFP-FisB cells at t=3 h after sporulation was induced. From
195 these same images, we estimated the total fluorescence of dim, mobile clusters (DMC)
196 and ISEP in *B. subtilis* cells as a sum of background-corrected pixel values (Figure 2C).
197 Using the average values of these total intensities, we estimate ~40 copies at the ISEP,
198 and ~12 per DMC from the calibration in Figure 2D. From the total intensity of cells (S1
199 Appendix Fig. 2E), we also estimate there are ~1000 FisB molecules per cell. Two
200 independent estimates, based on *B. subtilis* calibration strains[45] and quantitative
201 immunoblotting, resulted in slightly larger and smaller estimates of these copy numbers,
202 respectively (S1 Appendix and S1 Appendix Figs. 2, 3).

203 We tracked the DMC to estimate how rapidly they move. From the tracks, we calculated
204 the mean squared displacement (MSD) as a function of time (Figure 2E). The short-time
205 diffusion coefficient estimated from the MSD is $D_{DMC} \approx 2.8 \times 10^3\ \mathrm{nm}^2/\mathrm{s}$ (95%
206 confidence interval CI=$2.76 - 2.85 \times 10^3\ \mathrm{nm}^2/\mathrm{s}$). This value is comparable to the
207 diffusivity of FloA and FloT clusters of ~100 nm with $D \approx 6.9 \times 10^3$ and 4.1×10^3 μm²/s,
208 respectively[46]. By comparison, ISEP have $D_{ISEP} \approx 28\ \mathrm{nm}^2/\mathrm{s}$ (CI=$22.9 - 33.1\ \mathrm{nm}^2/\mathrm{s}$), two
209 orders of magnitude smaller.

210 We performed similar estimations of FisB copy numbers for the low expression strain
211 (BAL004) (S1 Appendix Fig. 4). We found ~160±66, 122±51, or 83±6 (±SD) copies per
212 cell using *B. subtilis* standards, DNA-origami, or the quantitative WB methods,
213 respectively. For the ISEP, we found 8±2, 6±2, or 5±3 (±SD) copies of mGFP-FisB
214 using the three approaches, respectively (S1 Appendix Table 1). About 6 % of the total
215 mGFP-FisB signal accumulated in ISEP, close to the ~4% in the native-expression
216 strain (S1 Appendix Fig. 4E). The DMC were too dim to quantify reliably. Assuming
217 DMCs to be ~3-fold dimmer than ISEP like in the native-expression strain, each DMC
218 would contain 2-3 mGFP-FisB, just below our detection limit. Interestingly, lowering the
219 total expression of FisB per cell ~8-fold resulted in a ~6-fold reduction in the average
220 number of FisB molecules found at the membrane fission site. Thus, only ~6 copies of
221 FisB are sufficient to mediate membrane fission, but only after some delay (Figure
222 1E,F).

223 In summary, ~40 FisB molecules accumulate at the fission site to mediate membrane
224 fission. Only 3-4 DMCs need to reach the fission site to provide the necessary numbers.
225 When FisB expression is lowered ~8-fold, ~6 FisB molecules accumulate at the
226 engulfment pole to mediate membrane fission, but fission takes longer.

227

228 **FisB localization and membrane fission are independent of cardiolipin,**
229 **phosphatidylethanolamine and flotillins**

230 To investigate how FisB is recruited to the membrane fission site, we began by testing a
231 potential role for the cell wall remodeling machinery, the protonmotive force, and the
232 membrane potential, and found none influenced FisB dynamics (S1 Appendix Results
233 and S1 Appendix Fig. 6).

234 We then tested whether lipid microdomains play a role in recruitment to the site of
235 fission. Previously, we reported that the recombinant, purified extracytoplasmic domain
236 (ECD, see Figure 4A) of FisB interacts with artificial lipid bilayers containing CL[23]. To
237 test if FisB-CL interactions could be important for the subcellular localization of FisB and
238 membrane fission, we generated a strain (BAM234) that carries deletions of the three
239 known CL synthase genes *ywnE (clsA)*, *ywjE (clsB)* and *ywiE (clsC)*[47] (Figure 3A). The
240 CL synthase-deficient strain did not contain detectable levels of CL at t=3 hours after
241 sporulation was initiated (Figure 3B). CL-deficient cells grew normally but had a
242 reduction in sporulation efficiency as assayed by heat-resistant (20 min at 80˚C) colony
243 forming units (S1 Appendix Table 2 and S1 Appendix Figure 5)[33]. A reduction in
244 sporulation efficiency measured in this manner can be due to a defect at one or several
245 steps during sporulation or germination. Importantly, the membrane fission time course
246 of *ΔclsABC* cells was indistinguishable from those of wild-type cells (Figure 3C,D),
247 indicating the defect in sporulation occurs at a stage after membrane fission. In addition,
248 mYFP-FisB localization and dynamics were similar in *ΔclsABC* (BAL037) and wild-type
249 (BAL002) cells (Figure 3F-H). The fraction of cells that had an ISEP, and the intensity of
250 the ISEP, reflecting the number of FisB molecules recruited to the membrane fission
251 site, were indistinguishable for wild-type and *ΔclsABC* cells (Figure 3G,H). We conclude
252 that CL is not required for the subcellular localization of FisB or membrane fission.

253 Next, we tested a potential role for phosphatidylethanolamine (PE), another lipid
254 implicated in membrane fusion and fission[48,49] and that forms microdomains[50]. We
255 deleted the *pssA* gene which encodes phosphatidylserine synthase that mediates the
256 first step in PE synthesis (Figure 3A) to generate cells lacking PE (strain BAL031,
257 Figure 3B). Kinetics of membrane fission during sporulation were identical in *ΔpssA* and
258 wild-type cells (Figure 3D), indicating PE does not play a significant role in membrane
259 fission.

260 PE and CL domains in *B. subtilis* membranes tend to occur in the same sub-cellular
261 regions[50], raising the possibility that CL and PE may compensate for each other. To test
262 whether removing both CL and PE affects fission, we generated a quadruple mutant
263 (BAL030) lacking both CL and PE (Figure 3B), leaving PG as the major phospholipid
264 component of the membrane. Surprisingly, the quadruple mutant underwent fission with
265 indistinguishable kinetics compared to wild-type (Figure 3C,D). Thus, two lipids with
266 negative spontaneous curvature and implicated in membrane fusion and fission
267 reactions in diverse contexts have no significant role in membrane fission mediated by
268 FisB during sporulation.

269 In addition to CL and PE microdomains, bacteria also organize many signal
270 transduction cascades and protein-protein interactions into functional membrane
271 microdomains (FMMs), loose analogs of lipid rafts found in eukaryotic cells[40]. The
272 FMMs of *B. subtilis* are enriched in polyisoprenoid lipids and contain flotillin-like
273 proteins, FloT and FloA, that form mobile foci in the plasma membrane[51,52]. FloT-
274 deficient cells have a sporulation defect, but which sporulation stage is impaired is not

275 known[46]. We observed that *ΔfloA* (BAL035), but not *ΔfloT* (BAL036), cells are impaired
276 in sporulation as assayed by heat-resistant colony forming units (S1 Appendix Table 2,
277 and S1 Appendix Figure 5). However, when we monitored engulfment and membrane
278 fission, we found both proceeded normally in *ΔfloA* cells (Figure 3D). Thus, the
279 sporulation defect in *ΔfloA* cells lies downstream of engulfment and membrane fission.
280 This was confirmed by blocking formation of FMMs during sporulation by addition of 50
281 μM zaragozic acid[53] to the sporulation medium which had no effect on the localization of
282 mGPF-FisB (Figure 3E).

283 Together, these results imply that FisB-mediated membrane fission that marks the end
284 of engulfment during sporulation is insensitive to the negative-curvature lipids CL, PE,
285 and to FloA/T-dependent lipid domains.

286

287 **FisB binds to acidic lipids**

288 PG can substitute for CL as a binding partner for many proteins[54,55]. To see if this might
289 also be the case for the FisB ECD, we quantified the affinity of this domain for both
290 lipids.

291 Most, but not all, algorithms (S1 Appendix Fig. 7) predict FisB to possess a single
292 transmembrane domain (TMD) with a small N-terminal cytoplasmic domain and a larger
293 (23-kDa) ECD, as depicted in Figure 4A. We first confirmed this predicted topology
294 using a cysteine accessibility assay[56] (S1 Appendix Fig. 8, Materials and Methods, and
295 S1 Appendix Results). Our attempts to determine the structure of recombinant, purified
296 FisB ECD were unsuccessful, but a computational model of FisB for residues 44 to 225,
297 covering most of the ECD is available[57] and is shown in Figure 4B. The model predicts
298 a curved ECD structure, with ~3 nm and ~5 nm for the inner and outer radii of
299 curvatures. The overall topology of FisB, with the predicted ECD structure is depicted in
300 Figure 4B.

301 We probed interactions of FisB ECD with PG using a liposome co-flotation assay,
302 illustrated in Figure 4C. Purified recombinant, soluble FisB ECD (Fig. 4A, bottom) was
303 incubated with liposomes and subsequently layered at the bottom of a discontinuous
304 density gradient. Upon equilibrium ultracentrifugation, the lighter liposomes float up to
305 the interface between the two lowest density layers together with bound protein, while
306 unbound protein remains at the bottom of the gradient. We collected fractions and
307 determined the percentage of protein co-floated with liposomes using SDS-PAGE and
308 densitometry, as shown in Figure 4D. We first determined that binding of FisB ECD to
309 liposomes containing CL was not dependent on pH or the divalent ion Ca^{2+} (S1
310 Appendix Fig. 9F,G). By contrast, the fraction of liposome-bound protein decreased
311 rapidly as the ionic strength increased (S1 Appendix Fig. 9H). These results indicated
312 binding was mainly electrostatic in nature.

313 At neutral pH, CL carries two negative charges, whereas PG and phosphatidylserine
314 (PS), a lipid not normally found in *B. subtilis*[58], carry only a single negative charge. If
315 binding is mediated mainly by electrostatic interactions, then liposomes carrying PG or
316 PS at two times the mole fraction of CL should bind nearly the same amount of FisB
317 ECD, since the surface charge density would be the same. Indeed, similar amounts of

318 FisB ECD were bound to liposomes carrying 30% CL, 60% PG, or 60% PS (Figure 4E).
319 FisB ECD did not bind neutral phosphatidylcholine PC liposomes[23].

320 To quantify the affinity of recombinant soluble FisB ECD for CL vs PG, we then titrated
321 liposomes containing 45 mole % CL or PG and measured binding of 100 nM FisB ECD
322 (Figure 4F). In these experiments, we used iFluor555 labeled FisB ECD (iFluor555-FisB
323 ECD) and detected liposome-bound protein using fluorescence rather than densitometry
324 of SYPRO-stained gels, which extended sensitivity to much lower protein
325 concentrations. The titration data were fit to a model to estimate the apparent
326 dissociation constant, K_d (see Materials and Methods), which was 1.0 μM for CL (95%
327 confidence interval CI=0.7-2.1 μM) and 3.6 μM for PG, respectively (CI=2.8-5.0, Figure
328 4F,G).

329 Together, these results suggest that while FisB has higher affinity for CL than for PG,
330 the higher affinity results mainly from the higher charge carried by CL. FisB does not
331 bind CL with much specificity; at the same surface charge density, FisB ECD binds PG,
332 or even PS which is not a *B. subtilis* lipid, with similar affinity. Thus, *in vivo* FisB is likely
333 to bind CL as well as PG which is much more abundant.

334

335 **Purified FisB ECD forms soluble oligomers**

336 FisB forms clusters of various sizes in cells as described above (Figure 1, 2) and does
337 not appear to have other protein interaction partners[23]. Thus, homo-oligomerization of
338 FisB may be important for its function. We explored oligomerization of recombinant,
339 soluble FisB ECD (Figure 5). When FisB ECD bearing a hexa-histidine tag is expressed
340 in *E. coli* and purified to homogeneity by affinity chromatography, samples analyzed by
341 SDS-PAGE show multiple bands corresponding to different oligomeric states (Figure 5D
342 and S1 Appendix Figure 9B). Size-exclusion chromatography (SEC) analysis resolved
343 the purified protein into predominant high molecular weight oligomeric structures eluting
344 over a wide range of sizes, and low molecular weight peaks comprising minor
345 components (Figure 5E and S1 Appendix Figure 9C, top). The minor peak at ~23 kDa
346 (18 ml elution volume) corresponds to monomeric FisB ECD, whereas the peak at ~400
347 kDa (15 ml) is FisB ECD that co-elutes with another protein, likely the 60 kDa
348 chaperone GroEL, a common contaminant in recombinant proteins purified from *E. coli*
349 (S1 Appendix Figure 9D). To rule out potential artefacts caused by the hexa-histidine
350 affinity tag, we also purified FisB ECD using a GST-tag, which yielded similar results.
351 The SEC of high molecular weight peaks collected from the initial chromatogram did not
352 show a redistribution when re-analyzed (S1 Appendix Figure 9C, bottom), suggesting
353 that once formed, the oligomeric structures are stable for an hour or longer.

354 We analyzed the high molecular-weight SEC fractions (peaks 1 and 2) using electron
355 microscopy (EM) after negative staining. This analysis revealed rod-like structures quite
356 homogeneous in size, ~50 nm long and ~10 nm wide (Figure 5F and S1 Appendix
357 Figure 9E). These structures displayed conformational flexibility, which precluded
358 structural analysis using cryoEM (and likely hampered our attempts to crystallize FisB
359 ECD). We estimate every rod-like oligomer can accommodate ~40 copies of the
360 predicted structure of $FisB^{44-225}$ shown in Figure 4B, similar to the number of FisB
361 molecules recruited to the membrane fission site in cells (Figure 2).

362

363 **A FisB mutant that is selectively impaired in homo-oligomerization**

364 To determine whether self-oligomerization and lipid-binding interactions are important
365 for FisB's function, we generated a series of mutants, characterized oligomerization and
366 lipid-binding of the mutant proteins *in vitro*, and analyzed FisB localization dynamics and
367 membrane fission during sporulation *in vivo*.

368 We suspected self-oligomerization of FisB was at least partially due to hydrophobic
369 interactions. Accordingly, we first mutated conserved residues G175, I176, I195 and
370 I196 in a highly hydrophobic region of FisB ECD (Figure 5A,B), producing a quadruple
371 mutant, G175A,I176S, I195T, I196S ($FisB^{GIII}$). These residues are on the surface of the
372 predicted structure of FisB ECD (Figure 5C), so are not expected to interfere with
373 folding. Purified $FisB^{GIII}$ ECD displayed reduced oligomerization when analyzed using
374 SDS PAGE or size exclusion chromatography (Figure 5D,E). Though much reduced in
375 amplitude, a broad, high molecular weight peak was still present in size exclusion
376 chromatograms (Figure 5E). Negative-stain EM analysis of this fraction revealed
377 oligomerization with less defined size and structure compared to wild type FisB ECD
378 (Figure 5G).

379 To test whether lipid binding of the GIII mutant was affected, we used the co-flotation
380 assay described above, except only two fractions were collected (Figure 5H,I). This
381 analysis revealed that, despite being impaired in self-oligomerization, $FisB^{GIII}$ ECD has
382 lipid binding properties similar to wild-type with a dissociation constant $K_d^{GIII} = 1.6$ μM
383 (95% confidence interval CI=0.9-5.1 μM), indistinguishable from that of wild type FisB
384 ECD^{WT} ($K_d^{wt} = 1.0\ \mu\mathrm{M}, \mathrm{CI} = 0.7 - 2.1\ \mu\mathrm{M}$, Figure 5J).

385

386 **$FisB^{K168D,K170E}$ ($FisB^{KK}$) is selectively impaired in binding acidic lipids**

387 To engineer lipid-binding mutants, we took advantage of our observation that FisB
388 binding to anionic lipids is principally mediated through electrostatic interactions (S1
389 Appendix Figure 9H). We generated a series of mutants in which we either neutralized
390 or inverted up to four charges (S1 Appendix Fig. 11 and S1 Appendix Table 2). The
391 ECD of a set of charge neutralization mutants were expressed in *E. coli*, purified and
392 tested for lipid binding using the liposome co-floatation assay. The largest reductions in
393 lipid binding were observed when lysines in a region comprising residues 168-172 were
394 neutralized (S1 Appendix Fig. 11A). This region corresponds to a highly positively
395 charged pocket in the predicted model of FisB 44-225 (Figure 5C).

396 A partially overlapping set of FisB mutants were expressed in a *ΔfisB* background and
397 tested for sporulation efficiency by monitoring formation of heat-resistant colonies (S1
398 Appendix Fig. 11B-E). Again, the strongest reductions in sporulation efficiency were
399 found when lysines 168, 170 or 172 were mutated (S1 Appendix Fig. 11D). We decided
400 to characterize the K168D, K170E mutation in more detail, as it produced the strongest
401 reduction in sporulation efficiency.

402 We purified the ECD of $FisB^{K168D,K170E}$ ($FisB^{KK}$) from *E. coli* and tested its binding to
403 liposomes containing 45 mole % CL using the co-floatation assay (Figure 5H-J). The

404 dissociation constant for FisB^{KK}-acidic lipid binding was $K_d^{KK} = 9.1$ μM (CI=6.5-15.3
405 μM), nearly 10-fold lower than that for wild-type FisB ECD ($K_d^{wt} = 1.0\ \mu\mathrm{M}, \mathrm{CI} = 0.7 -$
406 $2.1\ \mu\mathrm{M}$, Figure 5I,J). Importantly, formation of oligomers was not affected (Figure 5D,E).
407 Thus, FisB^{KK} is specifically impaired in binding to acidic lipids.

408

409 **FisB-lipid interactions and homo-oligomerization are important for targeting FisB**
410 **to the fission site**

411 Using the FisB mutants selectively impaired in binding to lipids or homo-oligomerization,
412 we investigated whether these activities are important for FisB's function *in vivo*. To
413 analyze FisB clustering and targeting to the fission site, we fused wild-type FisB or the
414 two mutants to an N-terminal monomeric YFP (mYFP) and expressed the fusions at
415 lower levels, which facilitated observation of ISEPs (Figure 6A). We induced these
416 strains to sporulate and monitored FisB dynamics and membrane fission. Both the lipid-
417 binding (FisB^{KK}) and the oligomerization mutant (FisB^{GIII}) were targeted to the cell
418 membrane, unlike many other mutants we tested (S1 Appendix Figure 11E and S1
419 Appendix Table 2). At t=1.5 h after the nutrient downshift, mYFP-FisB signals were
420 visible in all strains without any distinguishing features. At t=2.5 h, a subset of cells
421 expressing the wild-type FisB fusion had undergone membrane fission and these cells
422 had an ISEP. By contrast, membrane fission was not evident in either of the mutants.
423 By t=3 h, 25% of WT FisB cells had undergone fission, nearly always with an
424 accompanying ISEP. In the lipid binding FisB^{KK} mutant, only 8% of the sporulating cells
425 had accomplished membrane fission (Figure 6B), but more than 90% of those that did
426 had an ISEP (53/58 cells). Membrane fission events and the accompanying bright
427 mYFP-FisB spots were very rare (0.6%) in the oligomerization-deficient FisB^{GIII} mutant.

428 The distribution of fluorescence intensities of the foci from low-expression WT and KK
429 cells were indistinguishable (Figure 6C). Using the DNA-origami fluorescence intensity
430 calibration (Figure 2), we estimate 6±2 copies of low-expression FisB WT or the KK
431 mutant to have accumulated at the fission site. For the GIII mutant, there were not
432 enough cells with an intense spot to perform a similar analysis.

433 From TMA-DPH labeling, we determined the fraction of cells that successfully
434 completed fission as a function of time (Figure 6D). Oligomerization-deficient FisB^{GIII}
435 was not able to induce fission, whereas the lipid-binding mutant FisB^{KK} had a partial, but
436 severe defect (~50% reduction compared to wild-type). Importantly, both mutants were
437 expressed at levels similar to the wild-type (S1 Appendix Fig. 10), so the defects to form
438 an ISEP and undergo membrane fission are not due to lower expression levels.

439 Together, these results suggest FisB-lipid and FisB-FisB interactions are both important
440 for targeting FisB to the fission site.

441

442 ***C. perfringens* FisB can substitute for *B. subtilis* FisB**

443 So far, our results suggest FisB-FisB and FisB-acidic lipid interactions are the main
444 drivers for targeting FisB to the membrane fission site. If no other partners are involved,
445 FisB should be largely an independent fission module, i.e. FisB homologs from different

446 sporulating bacteria should be able to substitute for one another at least partially, even if
447 sequence homology is low outside the consensus region. To test this idea, we
448 expressed *Clostridium perfringens* FisB (FisB^{Cperf}) in *B. subtilis* cells lacking FisB
449 (BAL005). The sequence identity is only 23% between FisB sequences from these two
450 species. In the heat-kill assay, FisB^{Cperf} fully rescued *B. subtilis ΔfisB* defects (Figure
451 7A). *C. perfringens* FisB fused to mEGFP (mEGFP-FisB^{Cperf}) had similar dynamics as
452 FisB^{Bsubti}, forming DMCs at early times that gave way to an ISEP where membrane
453 fission occurs (Figure 7B). Population kinetics of membrane fission were slower with
454 FisB^{Cperf} (Figure 7C), but nearly every cell that underwent fission had an ISEP as for the
455 wild type protein (220/239, or 92%). The intensity distribution of mEGFP-FisB^{Cperf} ISEP
456 was shifted to smaller values compared to mEGFP-FisB^{Bsubti} ISEP (Figure 7D). Since
457 the average ISEP intensity for FisB^{Bsubti} corresponds to ~40 copies (Figure 2), we
458 deduce ~9 copies of FisB^{Cperf} accumulate at ISEP at the time of membrane fission. At
459 t=3 h into sporulation, the percentage of cells with an ISEP was lower for cells
460 expressing mEGFP-FisB^{Cperf} (Figure 7E).

461 In all conditions tested so far, nearly all cells that had undergone membrane fission also
462 had an intense FisB spot at the engulfment pole (Figs. 2,3,6, and 7). When we plotted
463 the percentage of cells having an ISEP against the percentage of cells that have
464 undergone fission at t=3 h, we found a nearly perfect correlation (Figure 7F). FisB^{Cperf} fit
465 this pattern well, despite having a low sequence identity to FisB^{Bsubti}, suggesting a
466 common localization and membrane fission mechanism, likely based on a few
467 conserved biophysical properties.

468

469 **FisB does not have a preference for highly curved membrane regions, but can**
470 **bridge membranes**

471 A number of proteins localize to sub-cellular sites due to their preference for curved
472 membrane regions[59-62]. During late stages of engulfment, the most highly curved region
473 in the cell is the membrane neck connecting the engulfment membrane with the rest of
474 the mother cell membrane and this is where FisB accumulates. We therefore asked
475 whether curvature-sensing could be a mechanism driving FisB's localization. To test this
476 possibility, we undertook three independent series of experiments.

477 First, we used the principle that any protein which preferentially binds curved
478 membranes at low membrane coverage can also induce membrane curvature when
479 present at sufficiently high coverage[60,63]. Thus, we tested whether the soluble ECD of
480 FisB could generate curved regions in highly malleable membranes of giant unilamellar
481 vesicles (GUVs) at high coverage. We incubated 2 μM purified soluble FisB ECD
482 labeled with iFluor555 with GUVs and monitored protein coverage and membrane
483 deformations using spinning-disc confocal microscopy. Even when the GUV
484 membranes were covered uniformly with iFluor555-FisB ECD we could not observe any
485 GUV membrane deformations (Figure 8A). As a positive control, we used purified
486 Endophilin A1 (EndoA1, labeled with Atto395), an N-BAR domain containing endocytic
487 protein[64-66]. We incubated 2 μM EndoA1 with GUVs composed of 45% DOPS, 24.5%
488 DOPC, 30% DOPE and 0.5% DiD, which resulted in extensive tubulation of GUV
489 membranes (Figure 8A), as reported previously[67]. Importantly, the difference in the

490 membrane sculpting ability of the two proteins is not due a weaker affinity of FisB ECD
491 for membranes ($K_d \approx 1$ μM for membranes with 45 mole % CL, Figure 4F) compared to
492 endophilin ($K_d = 1.15$ μM for membranes containing 45% DOPS, 30% DOPE, 24.5%
493 DOPC, 0.5% TR-DHPE[65]).

494 Second, we slowly deflated GUVs to facilitate any potential membrane curvature
495 generation by FisB ECD (which works against membrane tension) and/or to provide
496 curved regions to test if FisB ECD accumulated there. Deflated GUVs displayed curved
497 regions because their larger surface-to-volume ratios no longer allowed spherical
498 shapes. Even under these favorable conditions, FisB ECD was not able to generate
499 highly curved regions on these deflated GUVs (Figure 8B). In addition, if FisB ECD had
500 a preference for negatively (positively) curved regions, it should accumulate at such
501 regions while being depleted from positively (negatively) curved areas. Quantification of
502 FisB ECD coverage at negatively or positively curved membrane regions showed no
503 curvature preference (Figure 8B).

504 Third, we tested if FisB's localization in live *B. subtilis* cells depended on membrane
505 curvature. To avoid potentially confounding effects of other cues that may be present
506 during sporulation, we expressed GFP-FisB under an inducible promoter during
507 vegetative growth. In addition, we blocked cell division by inducing expression of MciZ[68].
508 MciZ normally blocks binary cell division during sporulation, but when expressed during
509 vegetative growth, cells grow into long flexible filaments that are bent to varying
510 degrees, providing regions with different membrane curvatures. We imaged GFP-FisB
511 spots along curved edges of these filaments and plotted the linear density of GFP-FisB
512 spots (spots/μm) as a function of filament curvature (Figure 8C). There was no clear
513 correlation between GFP-FisB spot density and filament curvature. Although this
514 method generates a limited amount of curvature, a similar approach was previously
515 used to show that DivIVA preferentially localizes to negatively curved regions[69].

516 In the GUV experiments, we noticed that FisB ECD caused GUVs to adhere to one
517 another when they came into contact, accumulating at the adhesion patch between the
518 membranes and at the rims (Figure 8D). Absorbance measurements using small
519 unilamellar vesicles (SUVs) confirmed that FisB ECD can bridge membranes and
520 aggregate liposomes (Figure 8E).

521 Overall, these experiments suggest that FisB does not have any intrinsic membrane
522 curvature sensing/sculpting ability, but it can bridge membranes.

523

524 **Modeling suggests self-oligomerization and membrane bridging are sufficient to**
525 **localize FisB to the membrane neck**

526 To test the hypothesis that the homo-oligomerization, lipid-binding and the unique
527 membrane topology could be sufficient to recruit FisB to the membrane neck, we
528 considered a minimal model based on free energy minimization. As depicted in Figure
529 9, we consider the free energy F of an axisymmetric membrane neck of radius R and
530 length L connecting two membrane sheets, corresponding to the local geometry where
531 the engulfment membrane meets the rest of the mother cell membrane. We assume the
532 surface density ϕ of FisB proteins in the neck is uniform and reaches equilibrium with a

surface density φ_0 of FisB in the surrounding membranes, and ask whether the neck geometry alone is enough to account for the observed FisB accumulation. The energy functional consists of a term accounting for membrane bending and tension, F_{m}, and another term accounting for FisB protein-protein interactions, F_{p}. We employ the classical Helfrich-Canham theory[70-75] for the energy of the membrane

$$F_{\mathrm{m}} = \int_{S_{\mathrm{n}}} dS_{\mathrm{n}} \left[\frac{\kappa}{2} H^2 + \gamma\right] + \int_{S_{\mathrm{s}}} dS_{\mathrm{s}} \gamma, \quad (1)$$

where S_{n} and S_{s} are the surfaces of the membrane neck and sheets, H is twice the mean curvature, κ is the bending modulus, and γ is the surface tension. The two membrane sheets are assumed to be planar, thus their only contribution to the energy comes from membrane tension.

For FisB, we include translational entropy, the energy of homo-oligomerization in trans between opposing membranes, and an energy that limits crowding. As shown above, FisB proteins do not exhibit curvature sensing, so we do not include a term coupling FisB density to membrane curvature in Eq. (1). This results in the following expression for the protein free energy

$$F_{\mathrm{p}} = \int_{S_{\mathrm{n}}} dS_{\mathrm{n}} \left\{k_{\mathrm{B}} T \phi \ln\left(\frac{\phi}{\phi_0}\right) + a V_{\mathrm{LJ}}(R) \phi^2 + U(\phi)\right\}, \quad (2)$$

where the first term accounts for translational entropy, the second term is an energy per unit area accounting for trans interactions of FisB, and which for simplicity is assumed to be proportional to the standard Lennard–Jones (LJ) potential accounting for a longer-range attraction and shorter-range repulsion,

$$V_{\mathrm{LJ}}(r) = \left(\frac{\sigma}{r}\right)^{12} - \left(\frac{\sigma}{r}\right)^{6}, \quad (3)$$

and finally $U(\phi)$ is an energy penalty for crowding that increases rapidly above a certain FisB concentration. To obtain $U(\phi)$ we assume a purely repulsive, truncated and shifted LJ potential between cis-neighboring FisB molecules, which we take to occupy a triangular lattice. Therefore, $U(\phi) = \epsilon\left[V_{\mathrm{LJ}}\left(r(\phi)\right) - V_{\mathrm{LJ}}(r_{\max})\right]$ when $r \leq r_{\max}$ and 0 when $r > r_{\max}$, where we have chosen $r_{\max} = 2^{1/6}\sigma_{\mathrm{cis}}$, namely the minimum of the LJ potential with length scale σ_{cis}. The result is

$$U(\phi) = \epsilon \frac{(\phi^3 - \phi_{r_{\max}}^3)^2}{4\phi_{r_{\max}}^6} \text{ for } \phi \geq \phi_{r_{\max}} \text{ or 0 for } \phi < \phi_{r_{\max}}, \quad (4)$$

Where $\phi_{r_{\max}} = 2^{\frac{2}{3}}/(3^{\frac{3}{2}}\sigma_{\mathrm{cis}}^2) = 2/(3^{\frac{3}{2}} r_{\max}^2)$ is the FisB concentration corresponding to a nearest neighbor distance $r_{\max}$.

We minimize $F = F_{\mathrm{m}} + F_{\mathrm{p}}$ with respect to ϕ to obtain an equation for the equilibrium density of FisB proteins in the neck

$$k_{\mathrm{B}} T \left[1 + \ln\left(\frac{\phi}{\phi_0}\right)\right] + 2a\phi \left[\left(\frac{\sigma}{R}\right)^{12} - \left(\frac{\sigma}{R}\right)^{6}\right] + \partial_\phi U(\phi) = 0. \quad (5)$$

Then, minimizing F with respect to R yields an equation that determines the equilibrium radius of the neck

$$\gamma_{\text{eff}} - \frac{\kappa}{2\,R^2} + a\phi^2\left[6\left(\frac{\sigma}{R}\right)^6 - 12\left(\frac{\sigma}{R}\right)^{12}\right] - \frac{2\gamma R}{L} = 0, \quad (6)$$

where $\gamma_{\text{eff}} = \gamma + k_B T\phi \ln\left(\frac{\phi}{\phi_0}\right) + U(\phi)$.

Figure 9B shows R and ϕ as functions of the FisB trans homo-oligomerization strength a, for different values of surface tension γ and neck length L. For realistic parameters (the dot), we find that FisB trans interactions are strong enough to stabilize the neck at R ~ 3 nm, with a close-packed concentration of FisB in the neck $\phi \approx \phi_{r_{\max}}$. For these same parameters, there is a critical lower limit of a below which the FisB interactions are too weak to stabilize the neck, so the neck opens, i.e. $R \to \infty$ in our simple model. Additionally, Figure 9B shows that the shorter the length of the neck L, the stronger the trans interactions needed to stabilize the neck at a finite radius. This makes intuitive sense: the longer the neck, the more FisB can be present to hold the neck together in opposition to membrane tension. (Note that expanding the radius of the neck actually decreases the total membrane area, which is the sum of the membrane in the neck and in the parallel sheets, so that surface tension tends to make the neck expand – see S2 Appendix).

While the above results suggest that an accumulation of FisB at the neck can be energetically stable, one question is how long it might take to reach that state? We expect nucleation of a critical cluster of FisB to be rate limiting, since the time required for diffusion and capture to reach ~40 FisB in the neck is quite short ~3.9 s (see S2 Appendix). To obtain a simple estimate of the nucleation time for both low-expression and native-expression strains, we assume that FisB proteins diffuse independently on the entire membrane and that nucleation of a stable cluster in the neck occurs when n proteins happen to be in the neck at the same time. To this end, we need to estimate the fraction of time there are n or more FisB in the neck, as well as the correlation time, i.e. the time between uncorrelated samples. Since we assume FisB proteins are independent, the number of proteins in the neck will be Poisson distributed, so we only need to know the average in the neck to obtain the full distribution. The average number of FisB in the neck is its area, $2\pi RL$, times the background concentration, ϕ_0. Furthermore, the correlation time is simply the time for a FisB to diffuse the length of the neck L^2/D. Using $\phi_0 \simeq 20$ FisB μm^{-2} (see "About 40 FisB molecules accumulate at the engulfment pole to mediate membrane fission" above) for the low-expression strain yields <FisB>$\simeq 0.03$ in the neck. Assuming that the one-hour delay in membrane fission during sporulation of low-expression strain is due to the time for nucleation, we can infer that the number of FisB proteins required for nucleation is $n \approx 3$ (see S2 Appendix). If the native-expression strain also needs $n \approx 3$ to nucleate, we can estimate its corresponding nucleation time using $\phi_0 \simeq 100$ FisB μm^{-2}, which yields <FisB>$\simeq 0.15$ and a nucleation time of ~ 30 s. We conclude that for native expression levels of FisB, nucleation of a stable cluster of FisB at the neck is not likely to be rate limiting for the process of membrane fission.

DISCUSSION

Previously, we showed that FisB is required for the membrane fission event that marks

610 the completion of engulfment of the forespore by the mother cell[23]. Here, we found that
611 a cluster of FisB molecules is nearly always present at the membrane fission site as
612 evidenced by an intense fluorescent spot at the engulfment pole (ISEP) using
613 fluorescently tagged FisB. The number of FisB molecules accumulated at the ISEP
614 correlates well with the fraction of cells having undergone membrane fission at a given
615 time point after induction of sporulation (Figs. 1,7). In addition, the number of wild-type
616 FisB molecules per ISEP correlates with the total number of FisB molecules per cell (S1
617 Appendix Figure 4). Thus, the kinetics of membrane fission is determined by the
618 accumulation of FisB molecules at the fission site. Lowering FisB expression could slow
619 membrane fission by slowing the accumulation of FisB at the pole, or by reducing the
620 number of FisB molecules driving fission after they are localized at the fission site. Our
621 modeling results are consistent with slower ISEP nucleation in the low-expression
622 strain, however, currently, we cannot experimentally distinguish between the two
623 possibilities, and both may be operating simultaneously.

624 How is FisB recruited to the fission site? Our results suggest FisB does not rely on
625 existing landmarks, lipid microdomains, cell-wall remodeling machinery, pH or voltage
626 gradients across the cell membrane, or membrane curvature cues for its dynamic
627 localization. In addition, we could not detect proteins interacting with FisB other than
628 itself using an anti-GFP resin pulling on YFP-FisB[23]. By contrast, we found self-
629 oligomerization and binding to acidic lipids to be critical for FisB's function, and purified
630 FisB ECD can bridge artificial membranes. Together, these results suggest FisB-FisB
631 and FisB-lipid interactions are key drivers for FisB clustering and accumulation at the
632 membrane fission site.

633 Can FisB oligomerization and lipid binding be sufficient to accumulate an immobile
634 cluster of FisB molecules at the engulfment pole? Modeling suggests this is indeed the
635 case. First, the narrow neck enables FisB's on opposing membranes to come close
636 enough to interact in trans. We infer this to be the preferred orientation for FisB-FisB
637 interaction, since otherwise large clusters would be expected to form elsewhere as well.
638 Second, the unique geometry of the neck connecting the engulfment membrane to the
639 rest of the mother cell membrane plays an important role, as this is the only region in
640 the cell where a cluster of FisB molecules can be "trapped", i.e., once a cluster is
641 formed inside the neck, it cannot diffuse away without breaking apart. This idea is
642 supported by the fact that we do not observe any FisB accumulation at the leading edge
643 of the engulfment membrane until a thin neck has formed at the end of engulfment.

644 The first FisB oligomers that appear during sporulation are dim, mobile clusters (DMCs),
645 each containing about a dozen FisB molecules. (One possibility is that the DMCs may
646 correspond to local membrane folds stabilized by FisBs interacting in trans.) Diffusion of
647 DMCs appears to be Brownian on the 10-20 s time scale (Figure 2), though a rigorous
648 analysis would require taking into account the geometry of the system. A DMC can
649 diffuse a typical distance of ~1 μm in ~ 5 min ($D_{DMC} \approx 3 \times 10^{-3} \mu m^2/s$, Figure 2E). By
650 comparison, engulfment in individual cells takes ~60 min on average[76]. Though the
651 engulfment time is much longer than the DMC diffusion time, the neck region, with an
652 inner diameter of several nanometers, only forms at the very end of the engulfment
653 process. Thus, ~40 FisB molecules could be recruited to the neck through diffusion-
654 limited capture of a few DMCs. However, we could not image such capture events

655 directly, and cannot rule out that FisB can also diffuse as monomers and could be
656 recruited to the neck in that form. Indeed, a simple model of the rate of nucleation of a
657 cluster of FisBs at the neck suggests that as few as three FisBs interacting in trans
658 could be sufficient to form a stable cluster there, with a nucleation time significantly
659 shorter than the engulfment time at native expression levels.

660 How many FisB molecules are needed for efficient membrane fission? In cells
661 completely lacking FisB, ~5% of the cells undergo membrane fission by t=3 h,
662 compared to ~80 % or ~30% for cells expressing FisB at native or ~8-fold reduced
663 levels, respectively (Figure 1F). The former achieve fission with ~40 copies, while the
664 latter with only ~6. Thus, FisB is not absolutely required for membrane fission, but it
665 makes it much more efficient, i.e. FisB catalyzes membrane fission. The variable
666 stoichiometry suggests that FisB does not oligomerize into a specific quaternary
667 structure with a definite stoichiometry. This variability appears to be a common property
668 among proteins catalyzing membrane fusion and fission, such as SNAREs[77-79] or
669 dynamin[14]. The smallest clusters associated with membrane fission had ~6 FisB copies
670 on average. This number is likely sufficient to form at least one ring inside the
671 membrane neck that eventually undergoes fission. Given that fission can occur in the
672 absence of FisB, it is likely that the FisB cluster cooperates with other cellular processes
673 to produce stress on this membrane neck.

674 We found FisB dynamics and membrane fission are not affected by removal of CL, PE,
675 or both. CL and PE are widely implicated in membrane fission and fusion reactions due
676 to their tendency to form non-bilayer structures[48,80-83]. The fact that CL or PE do not
677 affect membrane fission during sporulation is remarkable, because such lipids usually
678 affect the kinetics and/or the extent of fusion/fission reactions even if they are not
679 absolutely required[81]. We tested the role of CL in a strain that lacked all three known CL
680 synthases, with no detectable CL levels. A previous study reported that in *⊿clsABC B.*
681 *subtilis* cells, CL levels increase from undetectable during vegetative growth to readily
682 detectable during sporulation[31], suggesting a yet unidentified sporulation-specific CL
683 synthase may exist. Our results differ from those of Kawai et al. in that we were unable
684 to detect any CL in *⊿clsABC B. subtilis* cells during vegetative growth or sporulation. We
685 suggest the differences may be due to the different strain backgrounds used[84], PY79[85]
686 here vs. Bs168[86] in Kawai et al. or differences in detection sensitivities.

687 Overall, our results suggest FisB localizes to the membrane fission site using only lipid-
688 binding, homo-oligomerization, and the unique geometry encountered at the end of
689 engulfment. We propose that accumulation of a high enough density of FisB leads to
690 membrane fission, possibly by generating increased stress in the FisB network-
691 membrane composite, or in cooperation with another cellular process. A FisB
692 homologue with low sequence identity partially rescued fission defects in *ΔfisB B.*
693 *subtilis* cells, consistent with the idea that FisB acts as an independent module relying
694 mainly on homo-oligomerization, lipid-binding, and sporulation geometry.

695

696

697 **MATERIALS AND METHODS**

Materials

E. coli cardiolipin (CL), *E. coli* L-α-phosphatidylglycerol (PG), egg L-α-phosphatidylcholine (eggPC), *E.coli* L-α-phosphatidylethanolamine (PE), 1,2-dioleoyl-sn-glycero-3-phosphoethanolamine-N-(7-nitro-2-1,3-benzoxadiazol-4-yl) (NBD-PE), 1,2-dioleoyl-sn-glycero-3-phosphoethanolamine (DOPE), 1,2-dioleoyl-sn-glycero-3-phosphocholine (DOPC), 1,2-dioleoyl-sn-glycero-3-phospho-L-serine (DOPS) were purchased from Avanti Polar Lipids. 1-(4-Trimethylammoniumphenyl)-6-Phenyl-1,3,5-Hexatriene *p*-Toluenesulfonate (TMA-DPH) and *N*-(3-Triethylammoniumpropyl)-4-(6-(4-(Diethylamino) Phenyl) Hexatrienyl) Pyridinium Dibromide (FM4-64), and 1,1'-Dioctadecyl-3,3,3',3'-Tetramethylindodicarbocyanine (DiD) were from Thermo Fisher Scientific. Molybdenum Blue spray reagent was from Sigma-Aldrich. Carbonyl cyanide m-chlorophenyl hydrazone (CCCP) was purchased from Abcam and valinomycin was purchased from VWR. 3-(N-maleimidylpropionyl)biocytin (MBP) was obtained from Invitrogen and the HRP-conjugated antibody from eBioscience. Zaragozic acid was purchased from Sigma-Aldrich. 4-acetamido-4′-maleimidylstilbene-2,2′-disulfonic acid (AMS) and zaragozic acid were from obtained from Cayman Chemical Company.

General *B. subtilis* methods

B. subtilis strains were derived from the prototrophic strain PY79[85]. Sporulation was induced in liquid medium at 37°C by nutrient exhaustion in supplemented DS medium (DSM)[87] or by resuspension according to the method of Sterlini & Mandelstam[88]. Sporulation efficiency was determined in 24–30 h cultures as the total number of heat-resistant (80°C for 20 min) colony forming units (CFUs) compared to wild-type heat-resistant CFUs. Lipid synthesis mutants were from the *Bacillus* knock-out (BKE) collection[89] and all were back-crossed twice into *B. subtilis* PY79 before assaying and prior to antibiotic cassette removal. Antibiotic cassette removal was performed using the temperature-sensitive plasmid pDR244 that constitutively expresses Cre recombinase[89]. Cassette removal was further confirmed by PCR with primers flanking the deletion. *B. subtilis* strains were constructed using plasmidic or genomic DNA and a 1-step competence method. Site directed mutagenesis was performed using Agilent's Quick-change Lightning kit following manufacturer's instructions and mutations were confirmed by sequencing. The strains and plasmids used in this study are listed in S1 Appendix Tables 2 and 3, respectively.

Live-cell fluorescence microscopy of *B. subtilis*

Cells were mounted on a 2% agarose pad containing resuspension medium using a gene frame (Bio-Rad). Cells were concentrated by centrifugation (3300g for 30 s) prior to mounting and visualization. This step had no impact on the localization of the fusion proteins. Fluorescence microscopy was performed using a Leica DMi8 wide-field inverted microscope equipped with an HC PL APO 100×DIC objective (NA=1.40) and an iXon Ultra 888 EMCCD Camera from Andor Technology. Membranes were stained with TMA-DPH at a final concentration of 100 μM. Excitation light intensity was set to 50% and exposure times were 300 ms for TMA-DPH (λ_{ex}=395/25 nm; λ_{em}=460/50 nm); 500 ms for m(E)GFP (λ_{ex}=470/40; λ_{em}=500-550) and 1 s for mYFP (λ_{ex}=510/25; λ_{em}>530) respectively. Images were acquired with Leica Application Suite X (LAS X)

742 and analysis and processing were performed using the ImageJ software[90].

743 **Determination of FisB's topology**

744 We used the substituted cysteine accessibility method (SCAM[91]) to determine the
745 topology of FisB. We first generated stains expressing FisB versions with a single
746 cysteine substitution at position G6, L137, or A245, in a *ΔfisB* background. FisB does
747 not have any endogenous cysteines. These point mutations decreased the sporulation
748 efficiency slightly (S1 Appendix Table 2), we assume without affecting the topology. We
749 selectively biotinylated extra- or intracellular cysteines of *B. subtilis* protoplasts,
750 produced by addition of 0.5 mg/ml lysozyme and incubating cells at 37°C for 1h with
751 gentle rocking. Protoplasts were then incubated with the membrane-impermeant
752 reagent 3-(N-maleimidylpropionyl)biocytin (MBP). To selectively label extracellular
753 cysteines, protoplasts of sporulating cells at 2.5 h into sporulation were incubated with
754 100 µM MPB. The reaction was quenched with 50 mM DTT before cells were lysed with
755 hypotonic shock. To label intracellular cysteines selectively, extracellular cysteines of
756 protoplasts were first blocked AMS before cells were lysed and incubated with 100 µM
757 MPB. The reaction was quenched by addition of 100 µM MPB. FisB was pulled down
758 from the cell lysates as described in[91] using an anti-Myc antibody (mAb #2276) and
759 biotinylated proteins were detected by Western Blot using a HRP-conjugated-Avidin
760 antibody. Further details are provided in the S1 Appendix.

761 **Expression, purification, and labeling of recombinant FisB protein**

762 Recombinant soluble FisB ECD was purified as described in[23] but with slight
763 modifications. Briefly, His_6-FisB ECD was expressed in *E. coli* BL21 (DE3) from New
764 England Biolabs and purified using HisPur™ Ni-NTA Resin from Thermo Fisher
765 Scientific. Protein expression was induced with 1 mM IPTG at OD_{600} = 0.6 overnight at
766 16°C. Cells were harvested by centrifugation and the pellet was resuspended in Lysis
767 Buffer (20 mM HEPES, 500 mM NaCl, 0.5 mM TCEP, 20 mM Imidazole, 2% glycerol,
768 20 mM $MgCl_2$) and flash-frozen in liquid nitrogen. Pellets were thawed on ice and cells
769 were lysed by 5 passes through a high-pressure homogenizer (Avestin EmulsiFlex-C3).
770 The lysate was spun down at 100,000×g and the soluble fraction was incubated with
771 HisPur™ Ni-NTA Resin for 2.5 h at 4°C while rotating. The bound protein was washed
772 with Lysis Buffer, Lysis Buffer containing 50 mM and finally 100 mM Imidazole. The
773 protein was eluted in Elution Buffer (20 mM HEPES, 500 mM NaCl, 0.5 mM TCEP, 200
774 mM Imidazole, 2% glycerol, 20 mM MgCl2). The protein was concentrated using a
775 Vivaspin centrifugal concentrator with a 10 kDa molecular weight cutoff and the
776 concentration determined by Bradford protein assay. The protein was stored at -80ºC.

777 In experiments with labeled FisB ECD, we used a cysteine mutation, G123C (FisB ECD
778 does not have any endogenous cysteines). After expression and purification as above,
779 iFluor555-maleimide (AAT Bioquest) was reacted with FisB ECD^{G123C} following the
780 manufacturer's instructions. G123 is in a loop that if removed does not interfere with
781 FisB's function (S1 Appendix Figure 10).

782 **Analytical size-exclusion chromatography (SEC) and negative-stain electron**
783 **microscopy (EM)**

784 For SEC analysis His_6-FisB ECD was loaded onto a Superose 6 Increase 10/300 GL

785 column (GE) previously equilibrated with 20 mM HEPES, pH 7.5, 500 mM NaCl, 0.5 mM
786 TCEP, 2% glycerol, 20 mM $MgCl_2$, running at a flow rate of 0.5 ml/min at 4ºC. The
787 column was calibrated with Bio-Rad's Gel Filtration Standards. For negative stain EM
788 analysis, 4 µL of the indicated elution fractions were applied to 200-mesh copper grids
789 coated with ~10 nm amorphous carbon film, negatively stained with 2% (wt/vol) uranyl
790 acetate, and air-dried. Images were collected on a FEI Tecnai T12 microscope, with a
791 LaB6 filament operating at 120 kV, and equipped with a Gatan CCD camera.

792 **Inhibition of cell wall synthesis and analyses of FisB motions**

793 Overnight cultures of GFP-Mbl (BDR2061) or IPTG-induced mGFP-FisB (BMB014)
794 were diluted in CH medium to OD600 = 0.05. Expression of GFP-FisB was induced with
795 1 mM IPTG for 2h at 37°C. Expression of GFP-Mbl was induced with 10 mM xylose for
796 30 min when BDR2061 reached OD600 = 0.5. For imaging untreated cells, 1 ml of cells
797 was washed twice with 1 ml PBS and finally resuspended in 10 µl PBS. 2 µl of cell
798 suspension was spread on a 2% PBS agar pad for imaging. To inhibit cell-wall
799 synthesis 50 µg/ml fosfomycin was added to the cultures 45 min before imaging. 1 ml of
800 cells was washed twice with PBS containing 50 µg/ml fosfomycin and mounted on a
801 PBS agar pad also containing fosfomycin. Cells were imaged using a Olympus IX81
802 microscope with a home-built polarized TIRF setup[92,93]. Exposure times were 50 ms for
803 BDR2061 and 100 ms for BMB014. Movies were acquired at 1 frame/s. Movies
804 collected for BMB014 were corrected for bleaching using the Bleaching Correction
805 function (exponential method) in ImageJ. Kymographs were created with imageJ along
806 the indicated axes. GFP fusion proteins were tracked using the ImageJ plugin
807 TrackMate[94]. A Laplacian of Gaussian (LoG) filter was used to detect particles with an
808 estimated blob diameter 400 µm. Particles were tracked using the Simple LAP tracker
809 with a 0.25 µm maximum linking distance and no frame gaps. MATLAB (Mathworks,
810 Natick, MA) was used for further processing of the tracks. Mean squared displacement
811 (MSD) was calculated using the MATLAB class @msdanalyzer[95].

812 The asymmetry of individual tracks (S1 Appendix Fig. 5F) was calculated as described
813 in[96] using:

814 $$Asym = -log\left(1 - \frac{(R_1^2 - R_2^2)^2}{(R_1^2 + R_2^2)^2}\right)$$

815 where R_1 and R_2 are the principal components of the radius of gyration, equal to the
816 square roots of the eigenvalues of the radius of gyration tensor $\boldsymbol{R_g}$:

817 $$\boldsymbol{R_g}(\boldsymbol{i},\boldsymbol{j}) = \langle \boldsymbol{x_i}\boldsymbol{x_j}\rangle - \langle \boldsymbol{x_i}\rangle\langle \boldsymbol{x_j}\rangle.$$

818 **Tracking fluorescently labeled FisB spots and estimation of diffusion coefficients**

819 For estimating the mobility of DMC and ISEP, time-lapse movies were recorded with a
820 frame rate of 1 s using wide-field microscopy (50% LED intensity, 300 ms exposure
821 time, gain 300). Spot positions were tracked using SpeckleTrackerJ[97], a plugin for the
822 image analysis software ImageJ[90]. Mean-squared displacements (MSDs) were
823 calculated using the MATLAB class @msdanalyzer[95].

824 **Dissipation of membrane potential**

825 Cells were concentrated by centrifugation (3300xg for 30 s) and 100 μM CCCP or 30
826 μM valinomycin was added just prior to mounting cells onto a 2% PBS agar pad also
827 containing 100 μM CCCP or 30 μM valinomycin.

828 **Lipid extraction and thin-layer chromatography (TLC)**

829 Lipids were extracted from *B. subtilis* cells at 3 h into sporulation according to the
830 method of Lacombe and Lubochinsky[98]. Lipid extracts were analyzed by TLC on silica
831 gel plates in mixtures of chloroform:hexane:methanol: acetic acid (50:30:10:5).
832 Phospholipids were detected with Molybdenum Blue Reagent (Sigma-Aldrich).

833 **Liposome preparation**

834 Small unilamellar vesicles (SUVs) were prepared by mixing 1 μmol of total lipids at
835 desired ratios. A thin lipid film was created using a rotary evaporator (Buchi). Any
836 remaining organic solvent was removed by placing the lipid film under high vacuum for
837 2h. The lipid film was hydrated with 1 ml of RB-EDTA buffer [25 mM HEPES at pH 7.4,
838 140 mM KCl, 1 mM EDTA, 0.2 mM tris(2-carboxyethyl) phosphine] by shaking using an
839 Eppendorf Thermomix for >30 min. The lipid suspension was then frozen and thawed 7
840 times using liquid nitrogen and a 37°C water bath and subsequently extruded 21 times
841 through a 100 nm pore size polycarbonate filter using a mini-extruder (Avanti). All SUVs
842 contained 1% NBD-PE to determine the final lipid concentration.

843 Giant unilamellar vesicles (GUVs) were prepared by electroformation[99]. Briefly, lipids
844 dissolved in chloroform were mixed in a glass tube at desired ratios and spotted on two
845 indium tin oxide (ITO) coated glass slides. Organic solvent was removed by placing the
846 lipid films in a vacuum desiccator for at least 2 h. A short strip of copper conductive tape
847 was attached to each ITO slide which were then separated by a 3 mm thick
848 Polytetrafluoroethylene (PTFE) spacer and held together with binder clips. The chamber
849 was filled with 500 μl Swelling Buffer (1 mM HEPES, 0.25 M sucrose, 1 mM DTT) and
850 sealed with Critoseal (VWR International, Radnor, PA). GUVs were formed by applying
851 a 1.8 V sinusoidal voltage at 10 Hz for at least 2 h at room temperature.

852 For experiments involving FisB ECD the GUVs were composed of (all in mole
853 percentages): 25 *E. coli* PE, 5 *E. coli* CL, 50 *E. coli* PG, 19 eggPC and 1 DiD or 1 NBD-
854 PE. For experiments in which EndoA1 was used, GUV composition was (all in mole %):
855 45 DOPS, 24.5 DOPC, 30 DOPE and 0.5 DiD.

856 **Liposome-protein co-floatation**

857 For initial experiments, 40 nmol total lipid was incubated with 200 pmol FisB ECD for 1h
858 at room temperature in a total volume of 100 μl. 200 μl of 60% Optiprep (iodixanol,
859 Sigma-Aldrich) was added to the sample creating a 40% Optiprep solution. The sample
860 was then layered at the bottom of a 5 mm x 41 mm Beckman ultracentrifuge tube
861 (#344090) and overlaid with 200 μl of 20% Optiprep and finally 150 μl of buffer (Figure 4
862 C). Liposome-bound proteins co-float to a light density, while unbound proteins pellet
863 upon ultracentrifugation for 1.5 h at 48 krpm. Fractions were collected as shown in
864 Figure 4C and the amount of recovered protein was determined by SDS-PAGE (Nu-
865 PAPGE 12% Bis-tris gel, Thermo Fisher Scientific) stained with SYPRO™ Orange
866 (Invitrogen).

867 **Liposome aggregation using absorbance**

868 SUVs were prepared by extrusion as described above but using a 50 nm polycarbonate
869 filter. SUVs were composed of 50 mole % *E. coli* PG, 25 mole % *E. coli* PE, 20 mole %
870 eggPC, 5 mole % *E. coli* CL. The absorbance at 350 nm of 50 μM total lipid was
871 measured for 5 min, before addition of 1 μM FisB ECD. Absorbance increases with
872 increasing liposome aggregation due to increased scattering[100].

873 **Filamentous *B. subtilis* cells to test for curvature-sensitive localization of FisB**

874 An overnight culture of BMB014 was diluted into fresh CH medium[101] to OD_{600}=0.05. 1
875 mM IPTG and 20 mM xylose were added to induce the expression of GFP-FisB and
876 MciZ, respectively. The latter inhibits cytokinesis[68]. The culture was grown at 37°C for
877 30 min before 3-5 μl of cells were transferred onto a 3% agar pad also containing 1 mM
878 IPTG and 20 mM xylose. Cells were grown on the agar pad for 2h at 37°C prior to
879 imaging. GFP-FisB foci were detected using the ImageJ plugin TrackMate as described
880 above. Radii of the inner and outer edges were determined by manually fitting a circle to
881 the cells using ImageJ.

882 **Determination of binding constants**

883 For determination of binding constants, the floatation protocol was slightly modified.
884 Varying amounts of lipids were incubated with 100 nM iFluor555-FisB ECD for 1 h at
885 room temperature in a total volume of 100 μl. Density gradients were created as before
886 using Optiprep (iodixanol), however only 2 fractions were collected (Figure 5H). The
887 protein concentration in fraction A was too small to be quantified by SDS-PAGE.
888 Therefore, the sample was concentrated by trichloroacetic acid (TCA) precipitation.
889 Briefly, 50 μl of TCA was added to fraction A and incubated for 30 min at 4°C. The
890 sample was spun at 14 krpm in an Eppendorf microfuge for 5 min. The pellet was
891 washed twice with ice-cold acetone and subsequently dried for 10 min in a 95°C heating
892 block. 10 μl of 2X SDS sample buffer was added to the dried pellet and the sample was
893 boiled for 10 min at 95°C and loaded on a 12% bis-tris gel. The amount of recovered
894 protein was determined by fluorescence intensity of the labeled FisB ECD band on the
895 gel using a Typhoon FLA 9500 (GE Healthcare). The dissociation constant K_d was
896 determined following ref. 102. Titration curves were fitted to:

897 $$f_b = \frac{K[L]}{1+K[L]}, \qquad (1)$$

898 where f_b is the fraction of bound protein and K the apparent association constant ($K =$
899 $1/K_d$). Eq. (1) assumes that the total lipid concentration $[L]$ is much larger than the
900 concentration of bound protein, a condition satisfied in our experiments for $[L] > 10^{-7}$
901 M.

902 **Image analysis**

903 To estimate the fraction of cells that have undergone membrane fission at a particular
904 time after sporulation was initiated by nutrient downshift, cells were labeled with TMA-
905 DPH (see "Live-cell fluorescence microscopy of *B. subtilis*" above). The dye labels the
906 forespore contours intensely before membrane fission, as it has access to three
907 membranes in close proximity that cannot be resolved (forespore, engulfment, and
908 mother cell membranes). After membrane fission, the dye dimly labels forespore

909 contours (see S1 Appendix Fig. 1 for examples and quantification). Due to the clear
910 separation between the two labeling patterns (S1 Appendix Fig. 1) cells can be scored
911 visually, with 6-7% of cells having intermediate labeling that prevents categorization.
912 Thus, we underestimate the percentage of cells that have undergone membrane fission
913 by at most ~7%.

914 For the analyses shown in S1 Appendix Figs. 4A,B,C,E, and 9, we calculated the total
915 intensity (sum ox pixel values) inside the cell contour (indicated in yellow in Fig. S4A)
916 using MicrobeJ[103]. Mean integrated auto-fluorescence (~1300 a.u) was calculated by
917 analyzing in the same way an equivalent number of individual wild-type cells, imaged
918 under identical conditions.

919 For the analyses shown in Figure 2 and S1 Appendix Fig. 4D, FisB foci were semi-
920 automatically selected using SpeckleTrackerJ[97]. For each spot the sum of pixel values
921 in a 6 × 6 pixel (0.5 μm × 0.5 μm) box around the center of the spot were calculated. For
922 each corresponding cell the same operation was performed at a membrane area where
923 no clusters were present and subtracted from the FisB cluster intensity.

924 **Preparation of DNA Origami-based mEGFP standards**

925 These standards were prepared and characterized as described in[44]. Briefly, DNA
926 "rods" consisted of six-helix-bundle DNA origami nanotubes. Rods carried varying
927 numbers of single stranded “handle” sequences for DNA-conjugated fluorophore
928 hybridization. A long scaffold DNA (p7308[104]) was folded into the desired shape by self-
929 assembly with a six-fold molar excess of designed "staple strands" by heating and
930 cooling cycles over an 18-hour period in a thermocycler (Bio-Rad). Excess staples
931 were removed by PEG precipitation[105], and DNA-conjugated fluorophores were
932 hybridized to the DNA origami nanotubes by coincubation for 2 hours at 37ºC. Finally,
933 excess fluorophore-DNA conjugates were removed by a second PEG precipitation[105].
934 To estimate fluorophore labeling efficiency, standards designed to host 5 copies of
935 Alexa Fluor 488 were similarly prepared. These standards were imaged on a TIRF
936 microscope (Eclipse Ti, Nikon) until fully bleached. The photobleaching steps of the
937 fluorescence traces were fit to a binomial function to estimate the labeling efficiency to
938 be ~80% (95% CI = 76%-84%).

939 **Quantitative Western Blot**

940 mYFP was cloned into pVS001 (His_6-Sumo-mYFP) and purified using affinity
941 chromatography. For immunoblotting, cells in 100 ml sporulation medium were pelleted
942 and the supernatant removed. The pellets were suspended in ice-cold lysis buffer
943 (pH=7.5; 50 mM HEPES, 100 mM KCl, 3 mM $MgCl_2$, 1 mM EGTA, 0.1% Triton X-100, 1
944 mM DTT, 1 mM PMSF, with one complete protease inhibitor tablet (Roche) to a final
945 volume of 300 µl, and then we added 0.3 g acid-washed glass beads (425-600 µm,
946 Sigma). After adding 150 µl boiling sample buffer (250 mM Tris-HCl, pH 6.8, 50%
947 glycerol, 3.58 µM β-mercaptoethanol, 15% SDS, and 0.025% Bromophenol Blue),
948 samples were incubated at 100°C for 5 min. Samples were centrifuged at 14,000 rpm in
949 a desktop centrifuge at room temperature for 10 min and stored at -80°C. The blots
950 were probed with peroxidase-conjugated anti-GFP antibody (ab13970). Images were
951 scanned and quantified using ImageJ.

ACKNOWLEDGEMENTS

We thank members of the Karatekin and Rudner laboratories for stimulating discussions. This work was supported by National Institute of General Medical Sciences and National Institute of Neurological Disorders and Stroke of the National Institutes of Health (NIH) under award numbers R01GM114513 and R01NS113236 (to EK), DP2GM114830 and R01GM132114 (to CL). The content is solely the responsibility of the authors and does not necessarily represent the official views of the National Institutes of Health. We thank Vladimir Polejaev and Jeorg Nikolaus (directors of the Yale West Campus Imaging Core), and Josh Lees (Yale Center for Cellular and Molecular Imaging Electron Microscopy Facility) for their help with imaging, Karin Reinisch in whose laboratory work by FH was carried out, Daniel R. Zeigler (Bacillus Genetic Stock Center) for helpful advice, and Alexander J. Meeske for some of the strains used in this study. NDW was supported by a NIH training grant (T32-EB09941). We gratefully acknowledge a Yale University Predoctoral Fellowship to MB. This work was supported in part by the National Science Foundation, through the Center for the Physics of Biological Function (PHY-1734030). AM-C acknowledges support from the Spanish MECD through the program Ayudas para la Formación de Profesorado Universitario (FPU), Grant No. FPU16/0256. We are grateful to Aurelien Roux (U. Genève) for the generous gift of Atto395-EndoA1.

AUTHOR CONTRIBUTIONS

AL, MB, VS, and EK conceived the study. AL and MB performed experiments whose results are shown in the main figures. AA (Fig. S10), FH (Fig. 5, 7, S8), VS (Fig. S3) performed additional experiments. NDW and CL developed the DNA-origami fluorescence calibration method and contributed to the data in Fig. 2. CR, TD, and DR provided resources, training, and technical and conceptual input. They introduced EK, AL, MB and VS to *B. subtilis* and sporulation. EK and DR provided supervision and acquired funding. AMC and NW developed the model and wrote the corresponding sections. AL, MB, and EK and wrote the manuscript, with input from other co-authors. We thank Aurelien Roux for the generous gift of Atto395-EndoA1.

CONFLICT OF INTEREST

None.

FIGURE LEGENDS

Figure 1. Membrane fission during sporulation is nearly always accompanied by accumulation of a FisB cluster at the fission site. **A**. Vegetatively growing cells enter sporulation when nutrients become scarce. Asymmetric division creates a forespore (FS) and a mother cell (MC). The MC engulfs the FC in a phagocytosis-like event. At

993 the end of engulfment, a membrane neck connects the engulfment membrane to the
994 rest of the MC (i). Fission of the neck (ii) releases the FS, now surrounded by two
995 membranes, into the MC cytoplasm. Once the forespore becomes a mature spore, the
996 MC lyses to release it. **B**. The membrane fission step shown in more detail. **C**. Detection
997 of membrane fission. The lipophilic dye TMA-DPH does not fluoresce in the aqueous
998 solution and crosses membranes poorly. If membrane fission has not yet taken place,
999 the dye has access to the engulfment, FS and MC membranes, thus shows intense
1000 labeling where these membranes are adjacent to one another (i). If fission has already
1001 taken place, the dye labels internal membranes poorly (ii). **D.** Images show mGFP-FisB
1002 (strain BAM003, native expression level) at indicated times during sporulation.
1003 Membranes were visualized with TMA-DPH. Examples of sporulating cells with mGFP-
1004 FisB enriched at the septum (1.5 h), forming dim mobile cluster (DMC; 2 h) and with a
1005 discrete mGFP-FisB focus at the cell pole (intense spot at engulfment pole, ISEP, 3 h)
1006 are highlighted with arrowheads. **E.** Similar to D, but using a strain (BAL003) that
1007 expresses mGFP-FisB at lower levels in a *ΔfisB* background. **F.** Time course of
1008 membrane fission for wild-type cells, *ΔfisB* cells, or *ΔfisB* cells complemented with
1009 mGFP-FisB expressed at native (BAM003) or low levels (BAL003). Lower expression of
1010 mGFP-FisB leads to a delay in membrane fission kinetics. **G.** The percentage of cells
1011 with an intense spot at the engulfment pole (ISEP) for low and native level expression of
1012 mGFP-FisB as a function of time into sporulation. **H**. Correlation between percentage of
1013 cells that have undergone fission and percentage of cells having an ISEP for all time
1014 points shown in F and G. The fitted dashed line passing through the origin has slope
1015 1.06 ($R^2 = 0.9$). Scale bars represent 1 μm.

1016 **Figure 2. Estimation of mEGFP-FisB copies at the engulfment pole at t=3 h using**
1017 **DNA-origami calibration standards and mobility of FisB clusters**. **A.** Simplified
1018 schematic of the DNA-origami-based mEGFP standards used in this study. Using DNA
1019 origami, DNA rods bearing AF647 at both ends and the indicated numbers of mEGFP
1020 molecules along the rod were designed. In the actual rods, the labeling efficiency was
1021 found to be ~80%, so the actual copies of mEGFP per rod were 4, 20, 40, 56, and 80.
1022 **B.** Representative wide field images of the DNA-origami-based mEGFP standards used
1023 in this study. Bars are 1 μm. **C**. Distributions of total fluorescence intensities (sum of
1024 pixel values) for the intense spot at the engulfment pole (ISEP) and the dim, mobile
1025 clusters (DMC). Background was defined individually for every cell where an ISEP or
1026 DMC intensity measurement was performed. Examples are shown on the left. **D.** Total
1027 fluorescence intensity (sum of pixel values) for DNA-origami rods as a function of
1028 mEGFP copy numbers. The best fit line passing through the origin has slope 29.56
1029 au/mEGFP ($R^2 = 0.97$). The total intensity of the ISEP and DMCs correspond to ~40
1030 and ~12 copies of mEGFP respectively. **E.** Mean-squared displacement (MSD) as a
1031 function of delay time for DMCs (magenta) and ISEPs (blue). Cells expressing mGFP-
1032 FisB (strain BAM003) were imaged using time-lapse microscopy. Forty-five cells from
1033 10 different movies at t=2.5 hr and 30 cells from 10 different movies at t=3 hr after
1034 nutrient downshift were analyzed. (See S1 Appendix Movie 1 for a representative single
1035 bacterium at t=2.5 hrs showing several mobile DMCs and Movie 2 for a representative
1036 single bacterium at t=3 hrs showing an immobile ISEP.) Fits to the initial 25 s (~10 % of

1037 delays) yielded $D_{DMC} = 2.80 \pm 0.05 \times 10^3\ \mathrm{nm}^2/\mathrm{s}$ (± 95% confidence interval, R^2 = 0.999,
1038 24 tracks) and $D_{ISEP} = 2.80 \pm 0.51 \times 10\ \mathrm{nm}\hat{}2/\mathrm{s}$ (± 95% confidence interval, R^2 = 0.850,
1039 25 tracks). **F.** Summary of FisB copy number and cluster mobility estimation.

1040 **Figure 3. Membrane fission is insensitive to membrane lipid composition**. **A.**
1041 Pathways for membrane lipid synthesis in *B. subtilis*. Lipid synthetases responsible for
1042 each step are highlighted in blue. **B.** Thin-layer chromatography (TLC) of the total lipid
1043 extracts of wild-type and indicated lipid synthesis-deficient cells. Cells were collected 3
1044 hrs after induction of sporulation by nutrient downshift. Phospholipid spots (PLs) were
1045 visualized by staining with Molybdenum Blue spray reagent. Purified CL, PG, and PE
1046 were used as standards to identify the PLs of *B. subtilis*. Arrows indicate locations to
1047 which individual standards migrate. **C.** Membranes from cells of the indicated genetic
1048 backgrounds were visualized with TMA-DPH at t=3h. The images are from cells
1049 mounted on agarose pads containing sporulation medium. Bar,1 µm. **D.** Percentage of
1050 cells from indicated strains that have undergone membrane fission as a function of time
1051 after initiation of sporulation. For every strain, 150-220 cells from 3 independent
1052 experiments were analyzed at the indicated times during sporulation. **E.** mGFP-FisB
1053 (strain BAM003) treated with the squalene-synthase inhibitor zaragozic acid, imaged at
1054 t=3 h. **F.** Cells expressing mYFP-FisB (low expression levels) in either wild type
1055 (BAL002) or in a CL deficient strain (BAL037) at t=3h. Membranes were visualized with
1056 the fluorescent dye TMA-DPH. Examples of sporulating cells with a discrete mYFP-FisB
1057 focus at the cell pole (ISEP) are highlighted (white arrows). Foci were semi-
1058 automatically selected with SpeckletrackerJ[97]. **G.** The percentage of cells with an
1059 intense spot at engulfment pole for wild-type (BAL002) or cardiolipin-deficient (BAL037)
1060 mYFP-FisB expressing cells at t=3h (low expression). For each strain, 150-220 cells
1061 from 3 independent experiments were analyzed. **H.** Distributions of total fluorescence
1062 intensities (sum of pixel values) at ISEP for wild-type (BAL002) or cardiolipin-deficient
1063 (BAL037) mYFP-FisB cells at 3hr into sporulation. For every strain, 150 ISEPs were
1064 analyzed. Scale bars are 1 µm.

1065 **Figure 4**. **Binding of FisB ECD to acidic lipids. A**. Domain structure of FisB and its
1066 His_6-tagged extracytoplasmic domain (ECD) used in floatation experiments. **B.**
1067 Predicted model of $FisB^{44-225}$ comprising most of the ECD[57], schematically attached to
1068 the membrane. **C**. Schematic of the floatation assay. Liposomes (40 nmol total lipid)
1069 and FisB ECD (200 pmol) were incubated for 1 hour (total volume of 100 µl) at room
1070 temperature and layered at the bottom of an iodixanol density gradient. Upon
1071 ultracentrifugation, liposomes float to the top interface, whereas unbound protein
1072 remains at the bottom. Four fractions were collected as indicated and analyzed by SDS-
1073 PAGE. **D**. SYPRO orange stained gel of FisB ECD incubated with liposomes containing
1074 45 mole % CL. The percentage of recovered protein is determined by comparing the
1075 intensity of the band in fraction B to the input band intensity. **E**. Indistinguishable
1076 amounts of FisB ECD are recovered when FisB ECD is incubated with liposomes
1077 containing different acidic lipid species as long as the charge density is similar. CL30,
1078 PG60, PS60 indicate liposomes containing 30 mole % CL, 60 mole % PG and 60 mole
1079 % PS, respectively. CL carries 2 negative charges, whereas PG and PS carry one each.
1080 The rest of the liposome composition is PC. **F**. Fraction of liposome-bound iFluor555-
1081 labeled FisB ECD (iFluor555-FisB ECD, 100 nM) recovered after floatation as a function

1082 of lipid concentration. Titration curves were fit to $f_b = K[L]/(1 + K[L])$, where f_b is the
1083 bound fraction of protein, $[L]$ is the total lipid concentration (assumed to be ≫ [protein
1084 bound]), and $K = 1/K_d$ the apparent association constant, and K_d is the apparent
1085 dissociation constant. **G**. Best fit values for K_d were 1.0 μM for CL (95% confidence
1086 interval, CI=0.7-2.1 μM) and 3.6 μM for PG (CI=2.8-5.0 μM), respectively. iFluor555-
1087 FisB ECD (100 nM) was incubated with10^{-8} to 10^{-4} M lipids for 1 h at room temperature
1088 before flotation. Liposomes contained 45 mole % of CL or PG and 55% PC.

1089 **Figure 5. FisB mutants selectively impaired in oligomerization and membrane**
1090 **binding. A**. Mutated residues shown on the FisB domain structure. **B**. Kyle-Doolittle
1091 hydrophobicity profile of the FisB sequence for wild-type (WT), FisB K168D,K170E
1092 ($FisB^{KK}$), and FisB G175A,I176S, I195T, I196S ($FisB^{GIII}$) mutants. **C.** Mutations shown
1093 on the predicted model[57] of $FisB^{44-225}$. Residue conservation (top) and electrostatic
1094 potential (bottom) are mapped onto the structure. **D**. Western blot of cell lysates from *E.*
1095 *coli* cells expressing $FisB\text{-}ECD^{WT}$, $FisB\text{-}ECD^{GIII}$, or $FisB\text{-}ECD^{KK}$, probed with an anti-
1096 histidine antibody. High molecular weight bands in the WT and KK lanes are largely
1097 absent in the GIII lane, indicating $FisB^{GIII}$ is less prone to forming oligomers. **E**. Size-
1098 exclusion chromatography of FisB WT and the GIII and KK mutants. Intensities of high
1099 and low molecular weight peaks are reversed for FisB WT and the GIII mutant, whereas
1100 the KK mutant has a profile similar to WT. **F**. A fraction corresponding to the high-
1101 molecular peak in E (indicated by *) for FisB WT was collected and imaged using
1102 negative-stain electron microscopy (EM), which revealed flexible, elongated structures
1103 ~50 nm × 10 nm. **G**. A similar analysis for $FisB^{GIII}$ revealed more heterogeneous and
1104 less stable structures. Scale bars in F, G are 50 nm. **H**. Schematic of the floatation
1105 experiments to determine the apparent affinity of FisB mutants for liposomes containing
1106 acidic lipids. Experiments and analyses were carried out as in Figure 4, except only two
1107 fractions were collected. iFluor555-FisB ECD (100 nM) was incubated with10^{-8} to 10^{-4} M
1108 lipids for 1 h at room temperature before floatation. Liposomes contained 45 mole % of
1109 CL and 55% PC. **I**. Fraction of protein bound to liposomes as a function of total lipid
1110 concentration. Data was fitted to a model as in Figure 4F. The data and fit for FisB WT
1111 is copied from Figure 4F for comparison. **J.** Best fit values for K_d were 1.0 μM for WT
1112 (95% confidence interval, CI=0.7-2.1 μM), 9.1 μM for KK (CI=6.5-15.3 μM), and 1.6 for
1113 GIII (CI=0.9-5.1 μM), respectively**.**

1114 **Figure 6. FisB clustering and binding to acidic lipids are both required for ISEP**
1115 **formation and membrane fission. A.** Snapshots of sporulating *ΔfisB* cells expressing
1116 $mYPF\text{-}FisB^{WT}$ (BAL002), $mYPF\text{-}FisB^{KK}$ (BAL006), or $mYPF\text{-}FisB^{GIII}$ (BAL007), at low
1117 levels. For each time point after downshifting to the sporulation medium, cell
1118 membranes were labeled with TMA-DPH and images were taken both in the membrane
1119 (left) and the YFP (right) channels. By t=2.5 h, some foci at the engulfment pole (ISEP)
1120 are visible for WT cells that have undergone membrane fission (red boxes), but not for
1121 the KK or GIII mutants (white boxes). A small fraction of KK mutants (7.3%)
1122 accumulated FisB at the engulfment pole and underwent membrane fission at t=3h.
1123 Scale bars represent 1 μm. **B.** Percentage of cells with an intense spot at the
1124 engulfment membrane (ISEP) at t=3 h into sporulation, for WT FisB, $FisB^{KK}$, or $FisB^{GIII}$.
1125 For every strain, 200-300 cells from three independent experiments were analyzed at
1126 the indicated times during sporulation. **C**. Distribution of background-corrected

1127 integrated intensities (sum of pixel values) of ISEP fluorescence for *ΔfisB* cells
1128 expressing mYFP-FisB^{WT} or mYPF-FisB^{KK}. The distributions are indistinguishable.
1129 Since low-expression cells accumulate, on average, 6±2 FisB^{WT} molecules at the ISEP
1130 (Fig. S4D), so do FisB^{KK} cells. 175 and 68 ISEPs were analyzed for WT and KK mutant
1131 strains. **D**. Percentage of cells that have undergone membrane fission at the indicated
1132 time points. (For every strain, 200-300 cells from 3 independent experiments were
1133 analyzed at the indicated times during sporulation.)

1134 **Figure 7. *C. perfringens* FisB can substitute for *B. subtilis* FisB despite poor**
1135 **sequence identity. A.** Heat-resistant colony forming units for *ΔfisB* cells expressing *B.*
1136 *subtilis* (BAL001) or *C.perfringens* FisB (BAL005) at native levels, presented as a
1137 percentage of the WT sporulation efficiency. Results are shown as means ± SD for
1138 three replicates per condition. **B.** Snapshot of *ΔfisB* cells expressing mEGFP-
1139 FisB^{Cperfringens}. Aliquots were removed at the indicated times, membranes labeled with
1140 TMA-DPH, and both the TMA-DPH and the EGFP channels imaged after mounting into
1141 agar pads. White boxed areas are shown on an expanded scale in yellow boxes.
1142 Arrows indicate cells with ISEP that have undergone membrane fission. Bar, 1 μm. **C**.
1143 Percentage of cells that have undergone membrane fission as a function of sporulation
1144 time for wild-type cells, *ΔfisB* cells, *ΔfisB* cells expressing *B. subtilis* mEGFP-FisB at
1145 native levels, or *ΔfisB* cells expressing mEGFP-FisB^{Cperfringens}**.** The plots for the first
1146 three conditions are reproduced from Figure 1F for comparison. **D.** Distribution of
1147 background-corrected total fluorescence intensity of ISEP for *ΔfisB* cells expressing
1148 mEGFP-FisB^{Cperfringens} or mEGFP-FisB^{Bsubtilis} at native levels. From the calibration in
1149 Figure 2D, we estimate 9±7 FisB^{Cperfringens} per ISEP. The distribution for mEGFP-
1150 FisB^{Bsubtilis} is reproduced from Figure 2C for comparison. (150 and 93 ISEPs were
1151 analyzed for mEGFP-FisB^{Bsubtilis} and mEGFP-FisB^{Cperfringens}, respectively.) **E**.
1152 Percentage of cells with ISEP, for *ΔfisB* cells expressing mEGFP-FisB^{Cperfringens} or
1153 mEGFP-FisB^{Bsubtilis}. (For each strain, 200-300 cells from 3 independent experiments
1154 were analyzed.) **F**. Percentage of cells that have undergone membrane fission at t=3 h
1155 vs. the percentage of cells with ISEP at the same time point, for the conditions
1156 indicated. There is a nearly perfect correlation between these two quantities (the
1157 dashed line is a best-fit, $y = 1.03x, R^2 = 0.96$).

1158 **Figure 8. FisB does not sense or induce membrane curvature. A**. FisB ECD does
1159 not induce deformation of GUV membranes. Left: GUVs incubated with 2 μM iFluor555-
1160 labeled FisB ECD did not show any tubulation or invagination of the GUV membrane.
1161 GUVs were composed of (in mole %: 25 *E. coli* PE, 5 *E. coli* CL, 50 *E. coli* PG, 19
1162 eggPC, 1 NBD-PE). Right: incubation of 2 μM endophilin A1 (EndoA1, labeled with
1163 Atto395) with GUVs (45% DOPS, 24.5% DOPC, 30% DOPE and 0.5% DiD) resulted in
1164 extensive tubulation of membranes, as reported previously[22]. The two proteins have
1165 similar affinities for GUV membranes under these conditions (Figure 4F and ref. 106).
1166 **B**. FisB ECD cannot deform deflated GUVs and its membrane localization is
1167 independent of curvature. To avoid potential issues with high membrane tension
1168 preventing membrane deformation, GUVs were deflated using osmotic stress, which
1169 resulted in deformed GUVs with both negatively and positively curved regions. FisB
1170 ECD bound to these GUVs was unable to induce any high-curvature deformations. The
1171 intensity of iFluor555-FisB ECD along a membrane contour (proportional to coverage)
1172 was plotted against membrane curvature in the corresponding region. There was no

correlation between membrane curvature and FisB ECD coverage. **C**. FisB localization does not depend on curvature in filamentous *B. subtilis* cells. GFP-FisB was expressed under an inducible promoter during vegetative growth and cell division was blocked by inducing expression of MciZ[68]. Cells grew into long flexible filaments that were bent to varying degrees. The linear density of GFP-FisB spots (spots/μm) was independent of filament curvature. **D**. FisB ECD bridges GUV membranes. iFLuor555-FisB ECD (100 nM) was incubated with GUVs (same composition as in A and B). Many GUVs were found adhering to one another. iFluor555-FisB ECD signals were enhanced in the adhesion patches, in particular at the rims. Intensity profiles along the highlighted contours are shown below the examples. **E**. FisB ECD aggregates small liposomes. Liposomes (in mole %: 25 *E. coli* PE, 5 *E. coli* CL, 50 *E. coli* PG, 19 eggPC, 50 μM total lipid) were incubated in the absence and presence of FisB ECD (unlabeled) and their aggregation monitored by absorbance at 350 nm. FisB was added at 5 min (1 μM final), which caused the absorbance to increase, indicating increased liposome aggregation.

Figure 9. Modeling supports recruitment of FisB to membrane neck via oligomerization without curvature sensing. A. Left: Schematic of the late stages of engulfment, when a small membrane neck connects the engulfment membrane to the rest of the mother cell membrane. Right: Schematic of FisB accumulation at the fission site. FisB freely moves around the engulfment membrane and other regions of the mother cell membrane, forming clusters of up to ~12 molecules. Cluster motions are independent of lipid microdomains, flotillins, the cell-wall synthesis machinery, and voltage or pH gradients. About 40 copies of FisB accumulate at the membrane neck in an immobile cluster. Bottom: Modeled axisymmetric membrane neck of radius R and length L connecting two membrane sheets. The uniform areal concentration of FisB in the neck is ϕ. **B.** Top: Equilibrium radius of the neck as a function of FisB trans homo-oligomerization strength, a, for several values of neck length, L. Below a minimum interaction strength, FisB cannot stabilize the neck and the neck opens. The horizontal line is the radius corresponding to the minimum of the potential describing the trans interaction, $R = 2^{1/6}\sigma$ (Eq. 3). Bottom: Equilibrium FisB concentration in the neck as a function of a. The horizontal line is $\phi_{r_{\max}} = 2/(3^{3/2} r_{\max}^2)$, the concentration of FisB at the onset of in-plane crowding. Model parameters (see Eqs. 5 and 6): $\kappa = 20\ k_{\mathrm{B}}T$ (ref. 107), $\phi_0 = 100\ \mathrm{FisB}\ \mu\mathrm{m}^{-2}$, $\gamma = 10^{-4}\ \mathrm{N\ m}^{-2}$ (ref. [108]), $\sigma_{\mathrm{cis}} \simeq 2.47\mathrm{nm}$, $\phi_{r_{\max}} = 5 \times 10^4\ \mathrm{FisB}\ \mu\mathrm{m}^{-2}$, $L = 40\ \mathrm{nm}$, and for the dot $a \simeq 10^4\ k_{\mathrm{B}}T\ \mathrm{nm}^2\ \mathrm{FisB}^{-1}$. For details, see S2 Appendix.

REFERENCES

1. Haucke V, Kozlov MM. Membrane remodeling in clathrin-mediated endocytosis. *J Cell Sci* **131**, (2018).
2. Campelo F, Malhotra V. Membrane fission: the biogenesis of transport carriers. *Annu Rev Biochem* **81**, 407-427 (2012).
3. Ahmed I, Akram Z, Iqbal HMN, Munn AL. The regulation of Endosomal Sorting Complex Required for Transport and accessory proteins in multivesicular body

1216 sorting and enveloped viral budding - An overview. *Int J Biol Macromol* **127**, 1-11
1217 (2019).
1218 4. Jaumouille V, Waterman CM. Physical Constraints and Forces Involved in
1219 Phagocytosis. *Front Immunol* **11**, 1097 (2020).
1220 5. Carlton JG, Jones H, Eggert US. Membrane and organelle dynamics during cell
1221 division. *Nat Rev Mol Cell Biol* **21**, 151-166 (2020).
1222 6. Errington J. Regulation of endospore formation in Bacillus subtilis. *Nat Rev*
1223 *Microbiol* **1**, 117-126 (2003).
1224 7. Higgins D, Dworkin J. Recent progress in Bacillus subtilis sporulation. *FEMS*
1225 *Microbiol Rev* **36**, 131-148 (2012).
1226 8. Tan IS, Ramamurthi KS. Spore formation in Bacillus subtilis. *Environ Microbiol*
1227 *Rep* **6**, 212-225 (2014).
1228 9. Rand RP, Parsegian VA. Mimicry and mechanism in phospholipid models of
1229 membrane fusion. *Annu Rev Physiol* **48**, 201-212 (1986).
1230 10. Wong JY, Park CK, Seitz M, Israelachvili J. Polymer-cushioned bilayers. II. An
1231 investigation of interaction forces and fusion using the surface forces apparatus.
1232 *Biophys J* **77**, 1458-1468 (1999).
1233 11. Kozlovsky Y, Kozlov MM. Membrane fission: model for intermediate structures.
1234 *Biophys J* **85**, 85-96 (2003).
1235 12. Bashkirov PV, Akimov SA, Evseev AI, Schmid SL, Zimmerberg J, Frolov VA.
1236 GTPase cycle of dynamin is coupled to membrane squeeze and release, leading
1237 to spontaneous fission. *Cell* **135**, 1276-1286 (2008).
1238 13. Kozlov MM, McMahon HT, Chernomordik LV. Protein-driven membrane stresses
1239 in fusion and fission. *Trends Biochem Sci* **35**, 699-706 (2010).
1240 14. Ferguson SM, De Camilli P. Dynamin, a membrane-remodelling GTPase. *Nat*
1241 *Rev Mol Cell Biol* **13**, 75-88 (2012).
1242 15. Schoneberg J, Lee IH, Iwasa JH, Hurley JH. Reverse-topology membrane
1243 scission by the ESCRT proteins. *Nat Rev Mol Cell Biol* **18**, 5-17 (2017).
1244 16. Simunovic M*, et al.* Friction Mediates Scission of Tubular Membranes Scaffolded
1245 by BAR Proteins. *Cell* **170**, 172-184 e111 (2017).
1246 17. Roux A, Cuvelier D, Nassoy P, Prost J, Bassereau P, Goud B. Role of curvature
1247 and phase transition in lipid sorting and fission of membrane tubules. *EMBO J*
1248 **24**, 1537-1545 (2005).
1249 18. Hatch AL, Gurel PS, Higgs HN. Novel roles for actin in mitochondrial fission. *J*
1250 *Cell Sci* **127**, 4549-4560 (2014).
1251 19. Yang C, Svitkina TM. Ultrastructure and dynamics of the actin-myosin II
1252 cytoskeleton during mitochondrial fission. *Nat Cell Biol* **21**, 603-613 (2019).
1253 20. Lacy MM, Ma R, Ravindra NG, Berro J. Molecular mechanisms of force
1254 production in clathrin-mediated endocytosis. *FEBS Lett* **592**, 3586-3605 (2018).
1255 21. Nickaeen M, Berro J, Pollard TD, Slepchenko BM. Actin assembly produces
1256 sufficient forces for endocytosis in yeast. *Mol Biol Cell* **30**, 2014-2024 (2019).
1257 22. Snead WT*, et al.* BAR scaffolds drive membrane fission by crowding disordered
1258 domains. *J Cell Biol* **218**, 664-682 (2019).
1259 23. Doan T*, et al.* FisB mediates membrane fission during sporulation in Bacillus
1260 subtilis. *Genes Dev* **27**, 322-334 (2013).

1261 24. Stragier P, Losick R. Molecular genetics of sporulation in Bacillus subtilis. *Annu*
1262 *Rev Genet* **30**, 297-241 (1996).
1263 25. Gest H, Mandelstam J. Longevity of microorganisms in natural environments.
1264 *Microbiol Sci* **4**, 69-71 (1987).
1265 26. Potts M. Desiccation tolerance of prokaryotes. *Microbiol Rev* **58**, 755-805 (1994).
1266 27. Ulrich N, Nagler K, Laue M, Cockell CS, Setlow P, Moeller R. Experimental
1267 studies addressing the longevity of Bacillus subtilis spores - The first data from a
1268 500-year experiment. *PLoS One* **13**, e0208425 (2018).
1269 28. Brown JK, Hovmøller MS. Aerial dispersal of pathogens on the global and
1270 continental scales and its impact on plant disease. *Science* **297**, 537-541 (2002).
1271 29. Eichenberger P*, et al.* The sigmaE regulon and the identification of additional
1272 sporulation genes in Bacillus subtilis. *J Mol Biol* **327**, 945-972 (2003).
1273 30. Mileykovskaya E, Dowhan W. Visualization of phospholipid domains in
1274 Escherichia coli by using the cardiolipin-specific fluorescent dye 10-N-nonyl
1275 acridine orange. *J Bacteriol* **182**, 1172-1175 (2000).
1276 31. Kawai F, Shoda M, Harashima R, Sadaie Y, Hara H, Matsumoto K. Cardiolipin
1277 domains in Bacillus subtilis marburg membranes. *J Bacteriol* **186**, 1475-1483
1278 (2004).
1279 32. Koppelman CM, Den Blaauwen T, Duursma MC, Heeren RM, Nanninga N.
1280 Escherichia coli minicell membranes are enriched in cardiolipin. *J Bacteriol* **183**,
1281 6144-6147 (2001).
1282 33. Kawai F, Hara H, Takamatsu H, Watabe K, Matsumoto K. Cardiolipin enrichment
1283 in spore membranes and its involvement in germination of Bacillus subtilis
1284 Marburg. *Genes Genet Syst* **81**, 69-76 (2006).
1285 34. Lewis RN, McElhaney RN. The physicochemical properties of cardiolipin bilayers
1286 and cardiolipin-containing lipid membranes. *Biochim Biophys Acta* **1788**, 2069-
1287 2079 (2009).
1288 35. Haines TH. A new look at Cardiolipin. *Biochim Biophys Acta* **1788**, 1997-2002
1289 (2009).
1290 36. Ortiz A, Killian JA, Verkleij AJ, Wilschut J. Membrane fusion and the lamellar-to-
1291 inverted-hexagonal phase transition in cardiolipin vesicle systems induced by
1292 divalent cations. *Biophys J* **77**, 2003-2014 (1999).
1293 37. Khalifat N, Puff N, Bonneau S, Fournier JB, Angelova MI. Membrane deformation
1294 under local pH gradient: mimicking mitochondrial cristae dynamics. *Biophys J* **95**,
1295 4924-4933 (2008).
1296 38. Romantsov T, Helbig S, Culham DE, Gill C, Stalker L, Wood JM. Cardiolipin
1297 promotes polar localization of osmosensory transporter ProP in Escherichia coli.
1298 *Mol Microbiol* **64**, 1455-1465 (2007).
1299 39. Romantsov T, Stalker L, Culham DE, Wood JM. Cardiolipin controls the osmotic
1300 stress response and the subcellular location of transporter ProP in Escherichia
1301 coli. *J Biol Chem* **283**, 12314-12323 (2008).
1302 40. Lopez D, Koch G. Exploring functional membrane microdomains in bacteria: an
1303 overview. *Curr Opin Microbiol* **36**, 76-84 (2017).
1304 41. Sharp MD, Pogliano K. An in vivo membrane fusion assay implicates SpoIIIE in
1305 the final stages of engulfment during Bacillus subtilis sporulation. *Proc Natl Acad*
1306 *Sci U S A* **96**, 14553-14558 (1999).

1307 42. Meyer P, Gutierrez J, Pogliano K, Dworkin J. Cell wall synthesis is necessary for
1308 membrane dynamics during sporulation of Bacillus subtilis. *Mol Microbiol* **76**,
1309 956-970 (2010).
1310 43. Doan T*, et al.* Novel secretion apparatus maintains spore integrity and
1311 developmental gene expression in Bacillus subtilis. *PLoS Genet* **5**, e1000566
1312 (2009).
1313 44. Williams ND*, et al.* DNA-Origami-Based Fluorescence Brightness Standards for
1314 Convenient and Fast Protein Counting in Live Cells. *Nano Lett* **20**, 8890-8896
1315 (2020).
1316 45. Guiziou S*, et al.* A part toolbox to tune genetic expression in Bacillus subtilis.
1317 *Nucleic Acids Res* **44**, 7495-7508 (2016).
1318 46. Donovan C, Bramkamp M. Characterization and subcellular localization of a
1319 bacterial flotillin homologue. *Microbiology* **155**, 1786-1799 (2009).
1320 47. Kunst F*, et al.* The complete genome sequence of the Gram-positive bacterium
1321 Bacillus subtilis. *Nature* **390**, 249-256 (1997).
1322 48. Chernomordik LV, Kozlov MM. Mechanics of membrane fusion. *Nat Struct Mol*
1323 *Biol* **15**, 675-683 (2008).
1324 49. Schmid SL, Frolov VA. Dynamin: functional design of a membrane fission
1325 catalyst. *Annu Rev Cell Dev Biol* **27**, 79-105 (2011).
1326 50. Nishibori A, Kusaka J, Hara H, Umeda M, Matsumoto K.
1327 Phosphatidylethanolamine Domains and Localization of Phospholipid Synthases
1328 in *Bacillus subtilis* Membranes. *Journal of Bacteriology* **187**, 2163-2174 (2005).
1329 51. Good MC, Zalatan JG, Lim WA. Scaffold proteins: hubs for controlling the flow of
1330 cellular information. *Science* **332**, 680-686 (2011).
1331 52. Langhorst MF, Reuter A, Stuermer CA. Scaffolding microdomains and beyond:
1332 the function of reggie/flotillin proteins. *Cell Mol Life Sci* **62**, 2228-2240 (2005).
1333 53. López D, Kolter R. Functional microdomains in bacterial membranes. *Genes Dev*
1334 **24**, 1893-1902 (2010).
1335 54. Sohlenkamp C, Geiger O. Bacterial membrane lipids: diversity in structures and
1336 pathways. *FEMS Microbiology Reviews* **40**, 133-159 (2015).
1337 55. Oliver PM, Crooks JA, Leidl M, Yoon EJ, Saghatelian A, Weibel DB. Localization
1338 of anionic phospholipids in Escherichia coli cells. *J Bacteriol* **196**, 3386-3398
1339 (2014).
1340 56. Bogdanov M, Heacock PN, Dowhan W. Study of polytopic membrane protein
1341 topological organization as a function of membrane lipid composition. *Methods*
1342 *Mol Biol* **619**, 79-101 (2010).
1343 57. Ovchinnikov S*, et al.* Protein structure determination using metagenome
1344 sequence data. *Science* **355**, 294-298 (2017).
1345 58. den Kamp JA, Redai I, van Deenen LL. Phospholipid composition of Bacillus
1346 subtilis. *J Bacteriol* **99**, 298-303 (1969).
1347 59. Updegrove TB, Ramamurthi KS. Geometric protein localization cues in bacterial
1348 cells. *Curr Opin Microbiol* **36**, 7-13 (2017).
1349 60. Simunovic M, Voth GA, Callan-Jones A, Bassereau P. When Physics Takes
1350 Over: BAR Proteins and Membrane Curvature. *Trends in Cell Biology* **25**, 780-
1351 792 (2015).

1352 61. Antonny B. Mechanisms of membrane curvature sensing. *Annu Rev Biochem* **80**,
1353 101-123 (2011).
1354 62. Baumgart T, Capraro BR, Zhu C, Das SL. Thermodynamics and mechanics of
1355 membrane curvature generation and sensing by proteins and lipids. *Annu Rev*
1356 *Phys Chem* **62**, 483-506 (2011).
1357 63. Sorre B*, et al.* Nature of curvature coupling of amphiphysin with membranes
1358 depends on its bound density. *Proc Natl Acad Sci U S A* **109**, 173-178 (2012).
1359 64. Kjaerulff O, Brodin L, Jung A. The structure and function of endophilin proteins.
1360 *Cell Biochem Biophys* **60**, 137-154 (2011).
1361 65. Chen Z, Zhu C, Kuo CJ, Robustelli J, Baumgart T. The N-Terminal Amphipathic
1362 Helix of Endophilin Does Not Contribute to Its Molecular Curvature Generation
1363 Capacity. *J Am Chem Soc* **138**, 14616-14622 (2016).
1364 66. Hohendahl A*, et al.* Structural inhibition of dynamin-mediated membrane fission
1365 by endophilin. *Elife* **6**, (2017).
1366 67. Shi Z, Baumgart T. Membrane tension and peripheral protein density mediate
1367 membrane shape transitions. *Nat Commun* **6**, 5974 (2015).
1368 68. Handler AA, Lim JE, Losick R. Peptide inhibitor of cytokinesis during sporulation
1369 in Bacillus subtilis. *Mol Microbiol* **68**, 588-599 (2008).
1370 69. Renner LD, Eswaramoorthy P, Ramamurthi KS, Weibel DB. Studying
1371 biomolecule localization by engineering bacterial cell wall curvature. *PLoS One* **8**,
1372 e84143 (2013).
1373 70. Canham PB. Minimum Energy of Bending as a Possible Explanation of
1374 Biconcave Shape of Human Red Blood Cell. *J Theor Biol* **26**, 61-& (1970).
1375 71. Helfrich W. Elastic Properties of Lipid Bilayers - Theory and Possible
1376 Experiments. *Z Naturforsch C* **C 28**, 693-703 (1973).
1377 72. Zhongcan OY, Helfrich W. Instability and Deformation of a Spherical Vesicle by
1378 Pressure. *Phys Rev Lett* **59**, 2486-2488 (1987).
1379 73. Zhongcan OY, Helfrich W. Bending Energy of Vesicle Membranes - General
1380 Expressions for the 1st, 2nd, and 3rd Variation of the Shape Energy and
1381 Applications to Spheres and Cylinders. *Phys Rev A* **39**, 5280-5288 (1989).
1382 74. Seifert U, Langer SA. Viscous Modes of Fluid Bilayer-Membranes. *Europhys Lett*
1383 **23**, 71-76 (1993).
1384 75. Seifert U. Configurations of fluid membranes and vesicles. *Adv Phys* **46**, 13-137
1385 (1997).
1386 76. Ojkic N, López-Garrido J, Pogliano K, Endres RG. Cell-wall remodeling drives
1387 engulfment during Bacillus subtilis sporulation. *Elife* **5**, (2016).
1388 77. Hernandez JM, Kreutzberger AJ, Kiessling V, Tamm LK, Jahn R. Variable
1389 cooperativity in SNARE-mediated membrane fusion. *Proc Natl Acad Sci U S A*
1390 **111**, 12037-12042 (2014).
1391 78. Mostafavi H*, et al.* Entropic forces drive self-organization and membrane fusion
1392 by SNARE proteins. *Proc Natl Acad Sci U S A* **114**, 5455-5460 (2017).
1393 79. Wu Z*, et al.* Dilation of fusion pores by crowding of SNARE proteins. *Elife* **6**,
1394 (2017).
1395 80. Stepanyants N, Macdonald PJ, Francy CA, Mears JA, Qi X, Ramachandran R.
1396 Cardiolipin's propensity for phase transition and its reorganization by dynamin-

1397 related protein 1 form a basis for mitochondrial membrane fission. *Mol Biol Cell*
1398 **26**, 3104-3116 (2015).
1399 81. Chernomordik LV, Kozlov MM, Melikyan GB, Abidor IG, Markin VS,
1400 Chizmadzhev YA. The shape of lipid molecules and monolayer membrane
1401 fusion. *Biochimica et Biophysica Acta (BBA) - Biomembranes* **812**, 643-655
1402 (1985).
1403 82. Cullis PR, de Kruijff B, Verkleij AJ, Hope MJ. Lipid polymorphism and membrane
1404 fusion. *Biochem Soc Trans* **14**, 242-245 (1986).
1405 83. Landajuela A*, et al.* Lipid Geometry and Bilayer Curvature Modulate
1406 LC3/GABARAP-Mediated Model Autophagosomal Elongation. *Biophysical*
1407 *journal* **110**, 411-422 (2016).
1408 84. Zeigler DR*, et al.* The origins of 168, W23, and other Bacillus subtilis legacy
1409 strains. *J Bacteriol* **190**, 6983-6995 (2008).
1410 85. Youngman PJ, Perkins JB, Losick R. Genetic transposition and insertional
1411 mutagenesis in Bacillus subtilis with Streptococcus faecalis transposon Tn917.
1412 *Proc Natl Acad Sci U S A* **80**, 2305-2309 (1983).
1413 86. Spizizen J. TRANSFORMATION OF BIOCHEMICALLY DEFICIENT STRAINS
1414 OF BACILLUS SUBTILIS BY DEOXYRIBONUCLEATE. *Proc Natl Acad Sci U S*
1415 *A* **44**, 1072-1078 (1958).
1416 87. Schaeffer P, Millet J, Aubert JP. Catabolic repression of bacterial sporulation.
1417 *Proc Natl Acad Sci U S A* **54**, 704-711 (1965).
1418 88. Sterlini JM, Mandelstam J. Commitment to sporulation in Bacillus subtilis and its
1419 relationship to development of actinomycin resistance. *Biochem J* **113**, 29-37
1420 (1969).
1421 89. Koo BM*, et al.* Construction and Analysis of Two Genome-Scale Deletion
1422 Libraries for Bacillus subtilis. *Cell Syst* **4**, 291-305.e297 (2017).
1423 90. Schneider CA, Rasband WS, Eliceiri KW. NIH Image to ImageJ: 25 years of
1424 image analysis. *Nat Methods* **9**, 671-675 (2012).
1425 91. Bogdanov M, Zhang W, Xie J, Dowhan W. Transmembrane protein topology
1426 mapping by the substituted cysteine accessibility method (SCAM(TM)):
1427 application to lipid-specific membrane protein topogenesis. *Methods* **36**, 148-171
1428 (2005).
1429 92. Stratton BS*, et al.* Cholesterol Increases the Openness of SNARE-Mediated
1430 Flickering Fusion Pores. *Biophys J* **110**, 1538-1550 (2016).
1431 93. Nikolaus J, Karatekin E. SNARE-mediated Fusion of Single Proteoliposomes
1432 with Tethered Supported Bilayers in a Microfluidic Flow Cell Monitored by
1433 Polarized TIRF Microscopy. *J Vis Exp*, (2016).
1434 94. Tinevez JY*, et al.* TrackMate: An open and extensible platform for single-particle
1435 tracking. *Methods* **115**, 80-90 (2017).
1436 95. Tarantino N*, et al.* TNF and IL-1 exhibit distinct ubiquitin requirements for
1437 inducing NEMO-IKK supramolecular structures. *J Cell Biol* **204**, 231-245 (2014).
1438 96. Huet S, Karatekin E, Tran VS, Fanget I, Cribier S, Henry JP. Analysis of transient
1439 behavior in complex trajectories: application to secretory vesicle dynamics.
1440 *Biophys J* **91**, 3542-3559 (2006).
1441 97. Smith MB, Karatekin E, Gohlke A, Mizuno H, Watanabe N, Vavylonis D.
1442 Interactive, computer-assisted tracking of speckle trajectories in fluorescence

1443 microscopy: application to actin polymerization and membrane fusion. *Biophys J*
1444 **101**, 1794-1804 (2011).
1445 98. Lacombe C, Lubochinsky B. Specific extraction of bacterial cardiolipin from
1446 sporulating Bacillus subtilis. *Biochim Biophys Acta* **961**, 183-187 (1988).
1447 99. Angelova MI, Dimitrov DS. Liposome Electroformation. *Faraday Discuss* **81**, 303-
1448 + (1986).
1449 100. Connell E, Scott P, Davletov B. Real-time assay for monitoring membrane
1450 association of lipid-binding domains. *Anal Biochem* **377**, 83-88 (2008).
1451 101. Sterlini JM, Mandelstam J. Commitment to Sporulation in Bacillus Subtilis and Its
1452 Relationship to Development of Actinomycin Resistance. *Biochem J* **113**, 29-+
1453 (1969).
1454 102. Buser CA, Sigal CT, Resh MD, McLaughlin S. Membrane binding of myristylated
1455 peptides corresponding to the NH2 terminus of Src. *Biochemistry* **33**, 13093-
1456 13101 (1994).
1457 103. Ducret A, Quardokus EM, Brun YV. MicrobeJ, a tool for high throughput bacterial
1458 cell detection and quantitative analysis. *Nat Microbiol* **1**, 16077 (2016).
1459 104. Douglas SM, Dietz H, Liedl T, Högberg B, Graf F, Shih WM. Self-assembly of
1460 DNA into nanoscale three-dimensional shapes. *Nature* **459**, 414-418 (2009).
1461 105. Stahl E, Martin TG, Praetorius F, Dietz H. Facile and scalable preparation of pure
1462 and dense DNA origami solutions. *Angew Chem Int Ed Engl* **53**, 12735-12740
1463 (2014).
1464 106. Chen ZM, Atefi E, Baumgart T. Membrane Shape Instability Induced by Protein
1465 Crowding. *Biophysical Journal* **111**, 1823-1826 (2016).
1466 107. Powers TR. Dynamics of filaments and membranes in a viscous fluid. *Rev Mod*
1467 *Phys* **82**, (2010).
1468 108. Ojkic N, Lopez-Garrido J, Pogliano K, Endres RG. Bistable Forespore
1469 Engulfment in Bacillus subtilis by a Zipper Mechanism in Absence of the Cell
1470 Wall. *Plos Comput Biol* **10**, (2014).

1471

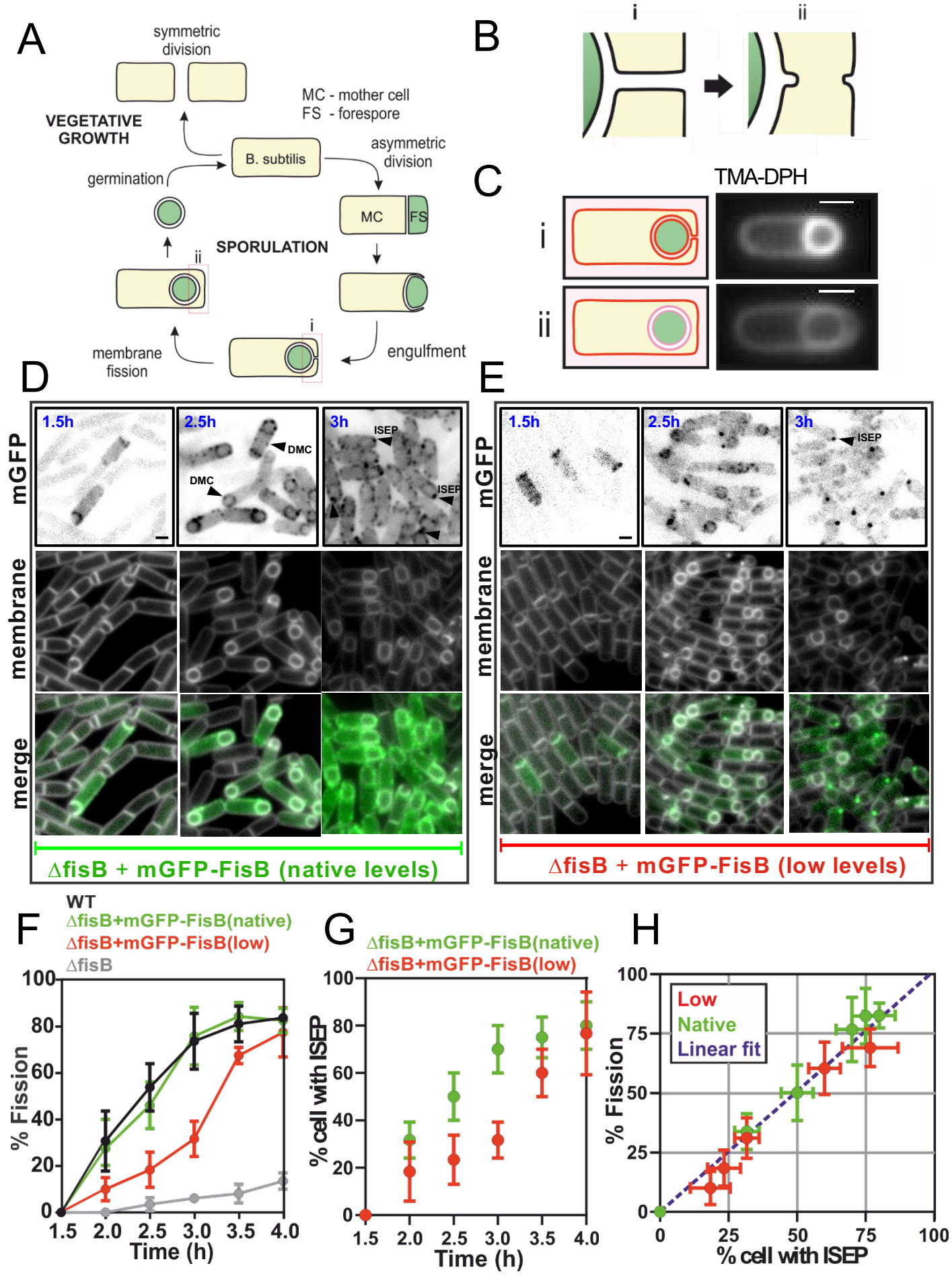
A
symmetric division
VEGETATIVE GROWTH
MC - mother cell
FS - forespore
B. subtilis
asymmetric division
germination
MC
FS
SPORULATION
ii
i
membrane fission
engulfment
B
i
ii
C
TMA-DPH
i
ii
D
mGFP
membrane
merge
1.5h
2.5h
3h
DMC
ISEP
ΔfisB + mGFP-FisB (native levels)
E
ΔfisB + mGFP-FisB (low levels)
F
WT
ΔfisB+mGFP-FisB(native)
ΔfisB+mGFP-FisB(low)
ΔfisB
% Fission
Time (h)
G
% cell with ISEP
H
Low
Native
Linear fit

FIGURE 1

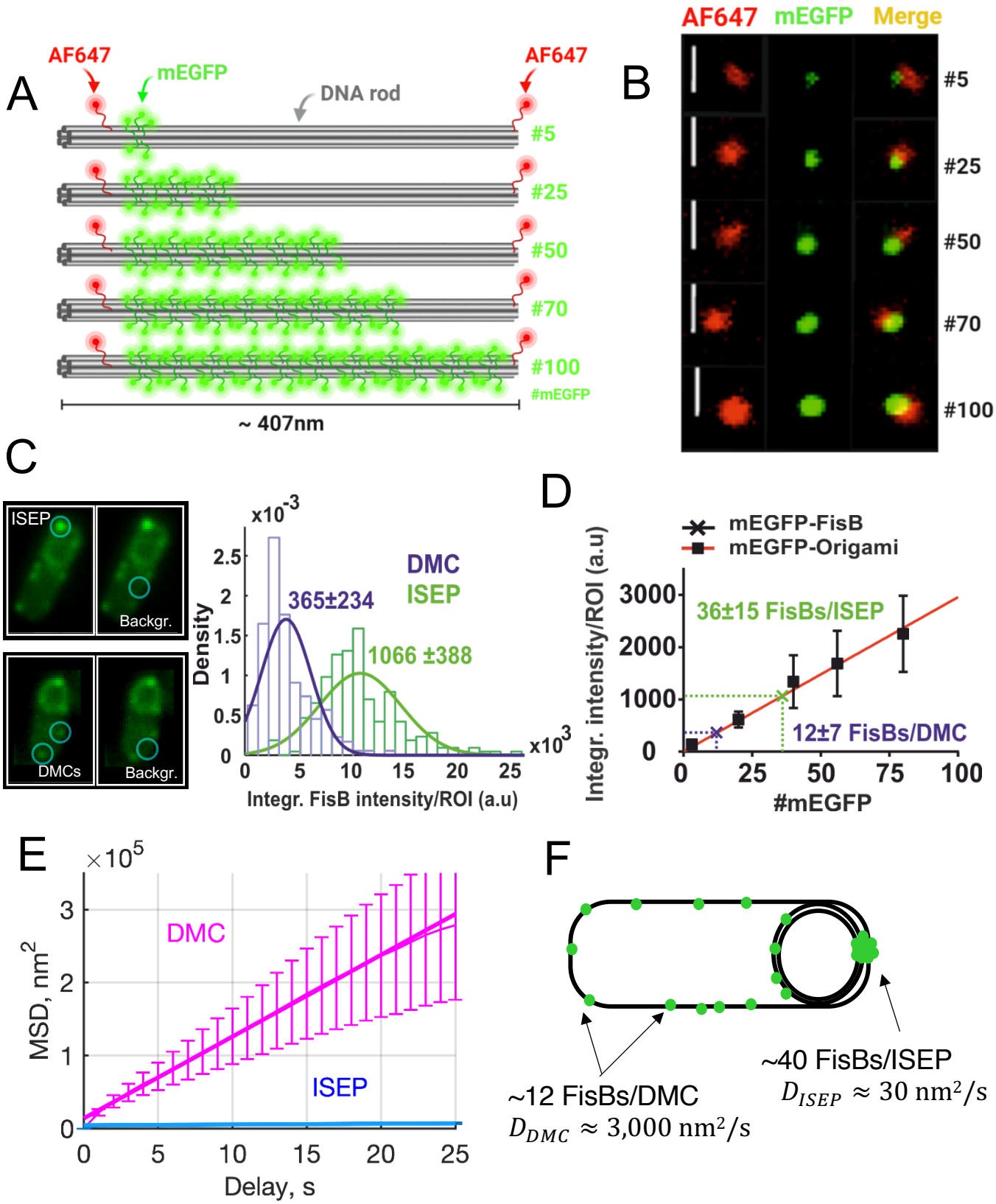
A
AF647
mEGFP
DNA rod
AF647
#5
#25
#50
#70
#100
#mEGFP
~ 407nm
B
AF647
mEGFP
Merge
#5
#25
#50
#70
#100
C
ISEP
Backgr.
DMCs
Backgr.
x10^-3
Density
365±234
DMC
ISEP
1066 ±388
x10^3
Integr. FisB intensity/ROI (a.u)
D
mEGFP-FisB
mEGFP-Origami
Integr. intensity/ROI (a.u)
36±15 FisBs/ISEP
12±7 FisBs/DMC
#mEGFP
E
×10^5
MSD, nm^2
DMC
ISEP
Delay, s
F
~12 FisBs/DMC
$D_{DMC} \approx 3{,}000\ \mathrm{nm}^2/\mathrm{s}$
~40 FisBs/ISEP
$D_{ISEP} \approx 30\ \mathrm{nm}^2/\mathrm{s}$

FIGURE 2

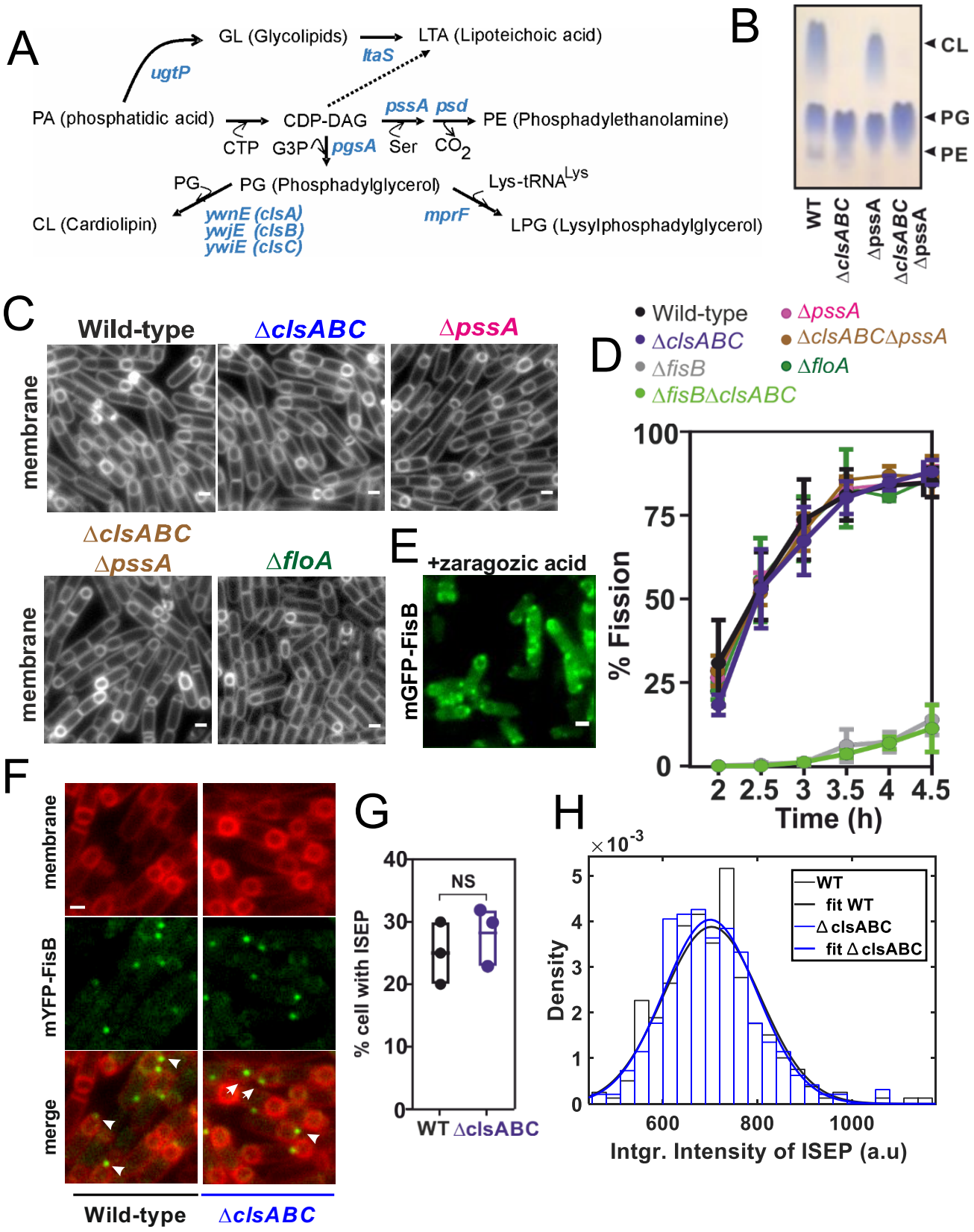
A
GL (Glycolipids)
LTA (Lipoteichoic acid)
ltaS
ugtP
PA (phosphatidic acid)
CDP-DAG
pssA psd
PE (Phosphadylethanolamine)
CTP G3P pgsA Ser CO2
PG
PG (Phosphadylglycerol)
Lys-tRNALys
CL (Cardiolipin)
ywnE (clsA)
ywjE (clsB)
ywiE (clsC)
mprF
LPG (Lysylphosphadylglycerol)
B
CL
PG
PE
WT
ΔclsABC
ΔpssA
ΔclsABC ΔpssA
C
Wild-type
ΔclsABC
ΔpssA
membrane
ΔclsABC ΔpssA
ΔfloA
E
+zaragozic acid
mGFP-FisB
D
Wild-type
ΔclsABC
ΔfisB
ΔfisBΔclsABC
ΔpssA
ΔclsABCΔpssA
ΔfloA
% Fission
Time (h)
F
membrane
mYFP-FisB
merge
Wild-type
ΔclsABC
G
% cell with ISEP
NS
WT ΔclsABC
H
×10-3
Density
WT
fit WT
Δ clsABC
fit Δ clsABC
Intgr. Intensity of ISEP (a.u)

FIGURE 3

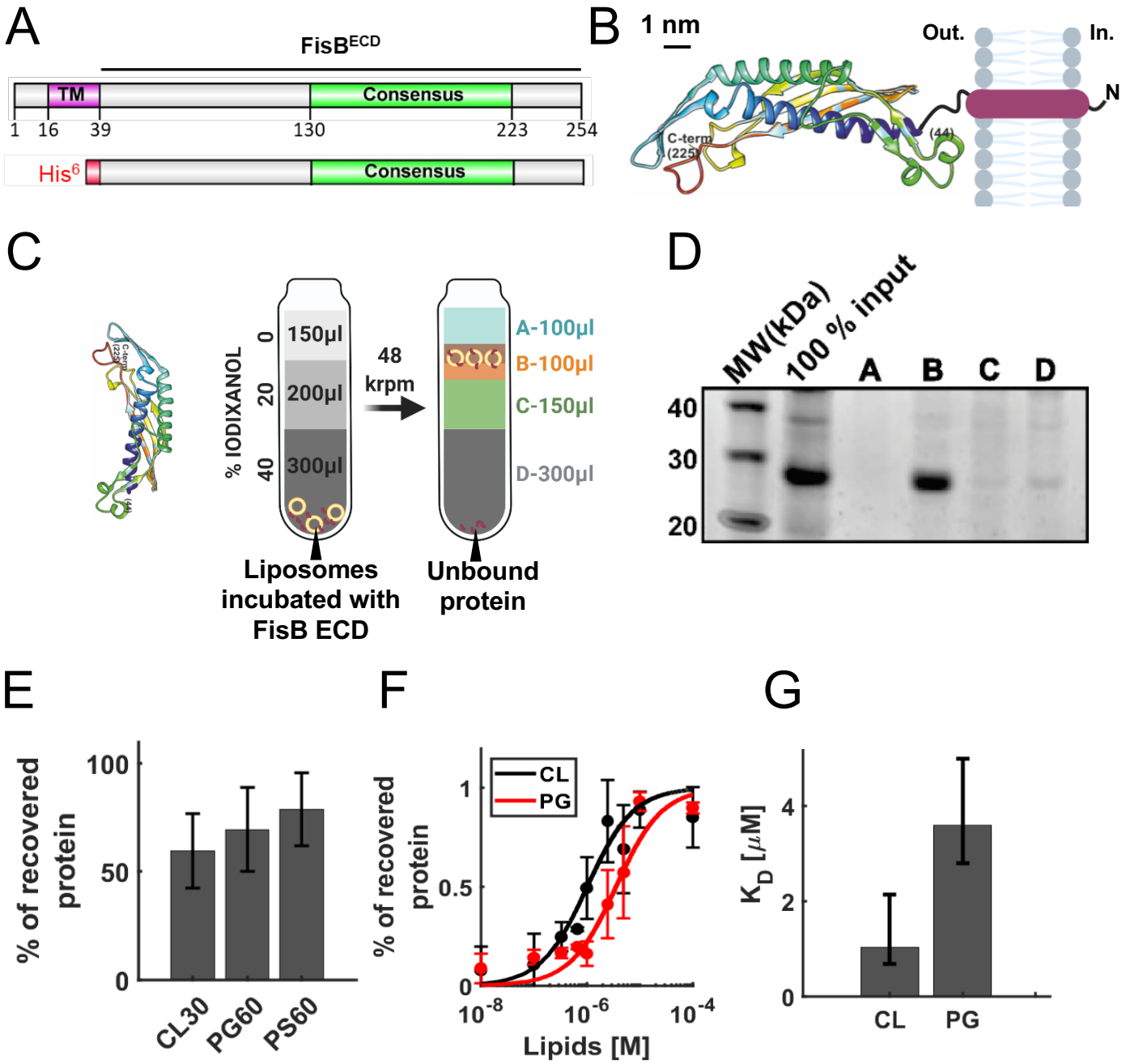
A
FisB^ECD
TM
Consensus
1
16
39
130
223
254
His6
Consensus
B
1 nm
Out.
In.
N
C-term
(225)
(44)
C
% IODIXANOL
0
20
40
150µl
200µl
300µl
48
krpm
A-100µl
B-100µl
C-150µl
D-300µl
Liposomes
incubated with
FisB ECD
Unbound
protein
D
MW(kDa)
100 % input
A
B
C
D
40
30
20
E
% of recovered
protein
100
50
0
CL30
PG60
PS60
F
% of recovered
protein
CL
PG
1
0.5
0
10^-8
10^-6
10^-4
Lipids [M]
G
K_D [µM]
4
2
0
CL
PG

FIGURE 4

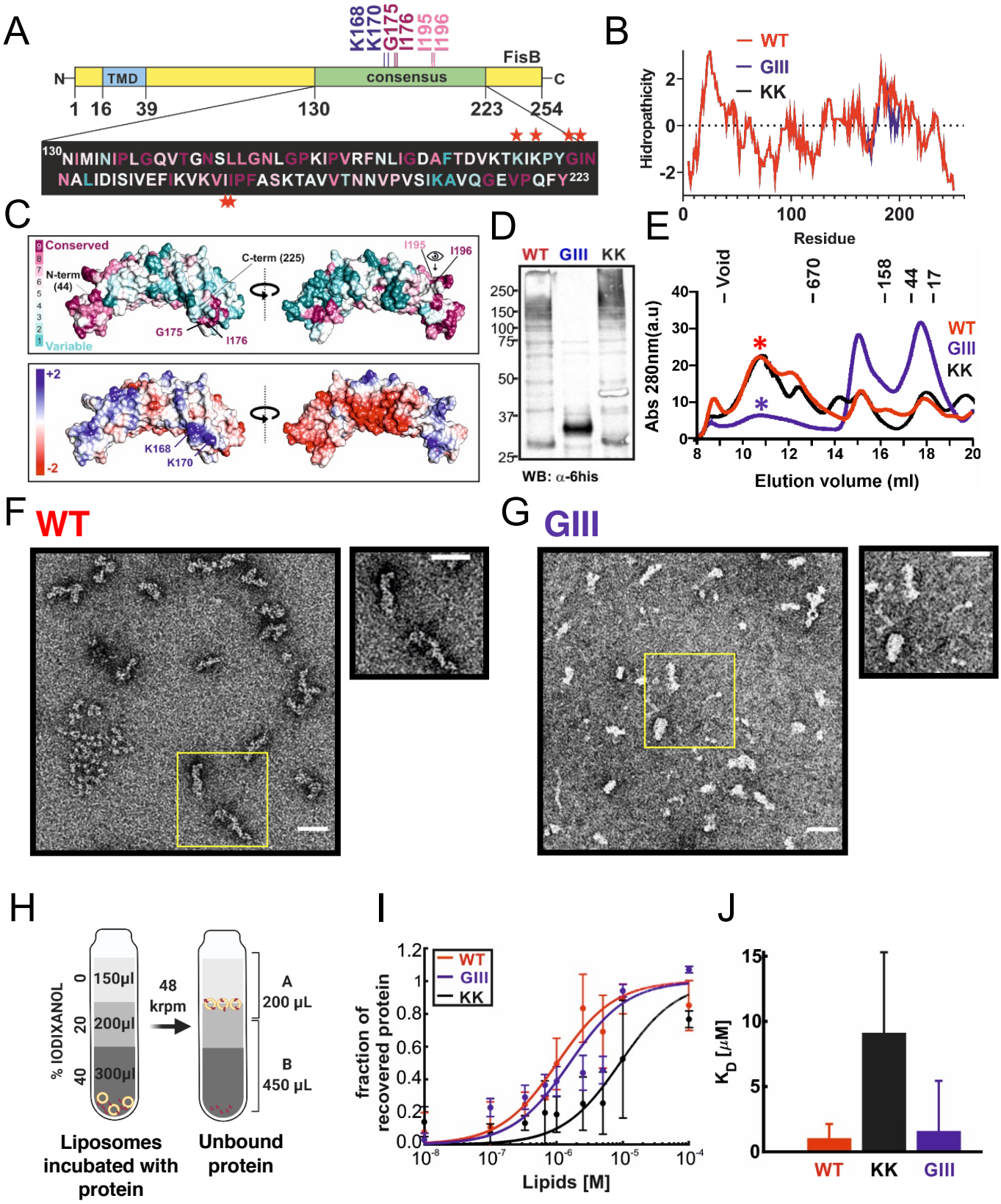
A
K168
K170
G175
I176
I195
I196
FisB
N
TMD
consensus
C
1 16 39 130 223 254
130 NIMINIPLGQVTGNSLLGNLGPKIPVRFNLIGDAFTDVKTKIKPYGIN
NALIDISIVEFIKVKVIIPFASKTAVVTNNVPVSIKAVQGEVPQFY 223
B
WT
GIII
KK
Hidropathicity
Residue
C
Conserved
Variable
N-term (44)
C-term (225)
G175
I176
I195
I196
K168
K170
+2
-2
D
WT GIII KK
250
150
100
75
50
37
25
WB: α-6his
E
Void
670
158
44
17
Abs 280nm(a.u)
Elution volume (ml)
WT
GIII
KK
F WT
G GIII
H
% IODIXANOL
0
20
40
150µl
200µl
300µl
48 krpm
A 200 µL
B 450 µL
Liposomes incubated with protein
Unbound protein
I
fraction of recovered protein
Lipids [M]
WT
GIII
KK
J
K_D [µM]
WT
KK
GIII

FIGURE 5

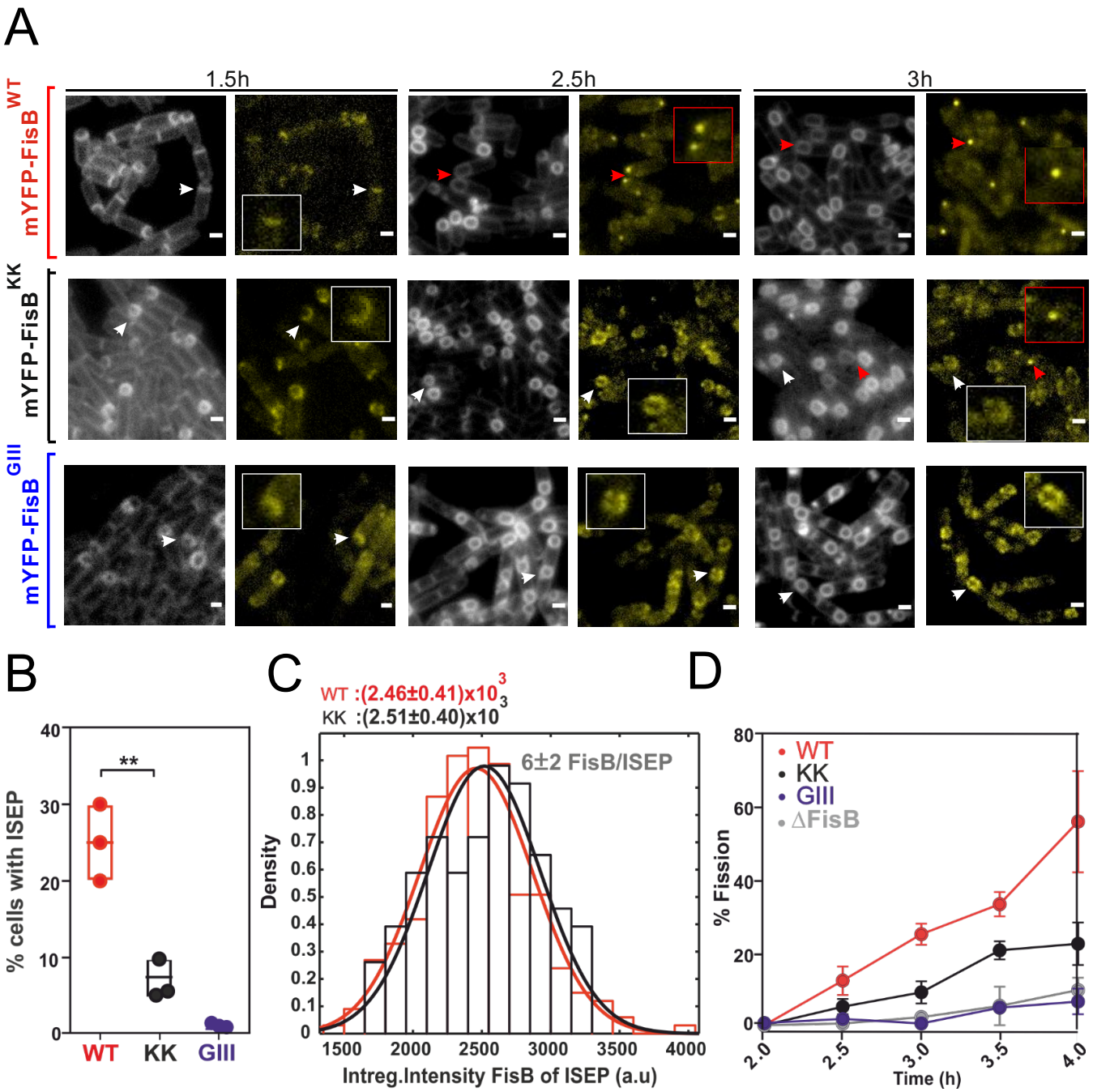
A
1.5h
2.5h
3h
mYFP-FisB WT
mYFP-FisB KK
mYFP-FisB GIII
B
% cells with ISEP
**
WT
KK
GIII
C
WT :(2.46±0.41)x10^3
KK :(2.51±0.40)x10^3
6±2 FisB/ISEP
Density
Intreg.Intensity FisB of ISEP (a.u)
D
WT
KK
GIII
ΔFisB
% Fission
Time (h)

FIGURE 6

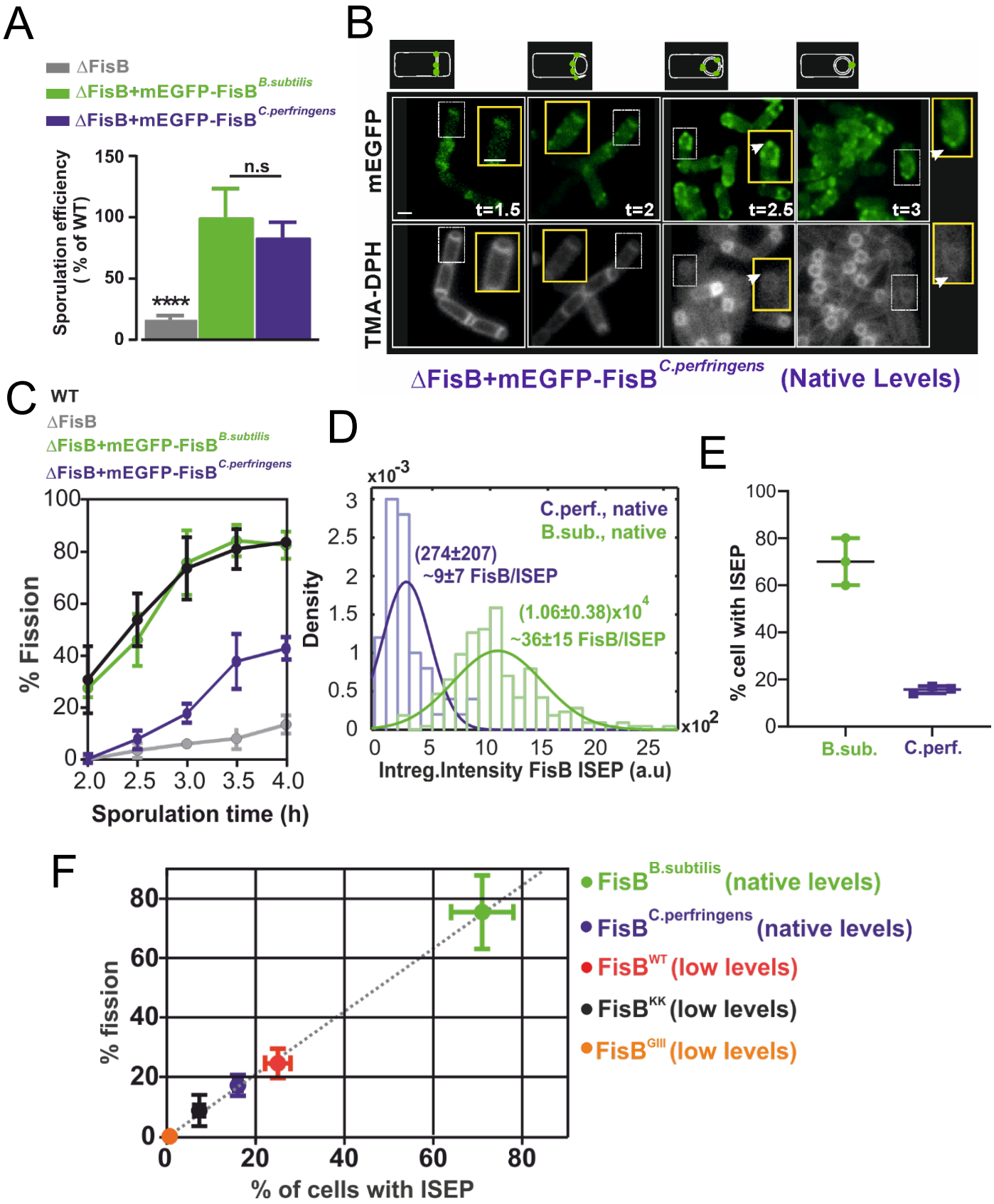
A
ΔFisB
ΔFisB+mEGFP-FisB B.subtilis
ΔFisB+mEGFP-FisB C.perfringens
Sporulation efficiency (% of WT)
150
100
50
0
n.s
****
B
mEGFP
TMA-DPH
t=1.5
t=2
t=2.5
t=3
ΔFisB+mEGFP-FisB C.perfringens (Native Levels)
C
WT
ΔFisB
ΔFisB+mEGFP-FisB B.subtilis
ΔFisB+mEGFP-FisB C.perfringens
% Fission
Sporulation time (h)
D
x10-3
C.perf., native
B.sub., native
(274±207)
~9±7 FisB/ISEP
(1.06±0.38)x10^4
~36±15 FisB/ISEP
Density
x10^2
Intreg.Intensity FisB ISEP (a.u)
E
% cell with ISEP
B.sub.
C.perf.
F
% fission
% of cells with ISEP
FisB B.subtilis (native levels)
FisB C.perfringens (native levels)
FisB WT (low levels)
FisB KK (low levels)
FisB GIII (low levels)

FIGURE 7

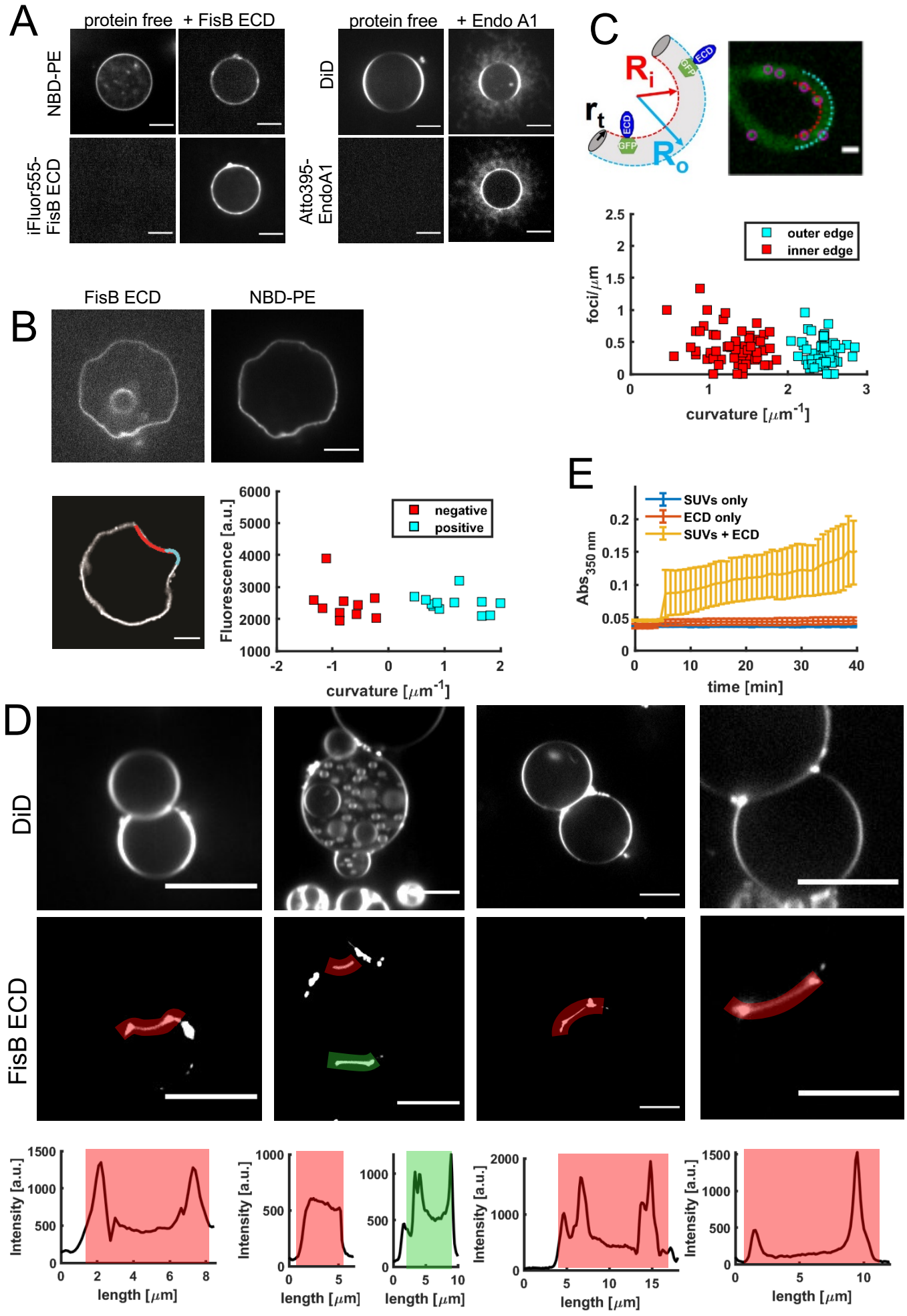
A
protein free
+ FisB ECD
NBD-PE
iFluor555-FisB ECD
protein free
+ Endo A1
DiD
Atto395-EndoA1
B
FisB ECD
NBD-PE
Fluorescence [a.u.]
negative
positive
curvature [μm-1]
C
Ri
Ro
rt
ECD
GFP
foci/μm
outer edge
inner edge
curvature [μm-1]
E
SUVs only
ECD only
SUVs + ECD
Abs350 nm
time [min]
D
DiD
FisB ECD
Intensity [a.u.]
length [μm]

FIGURE 8

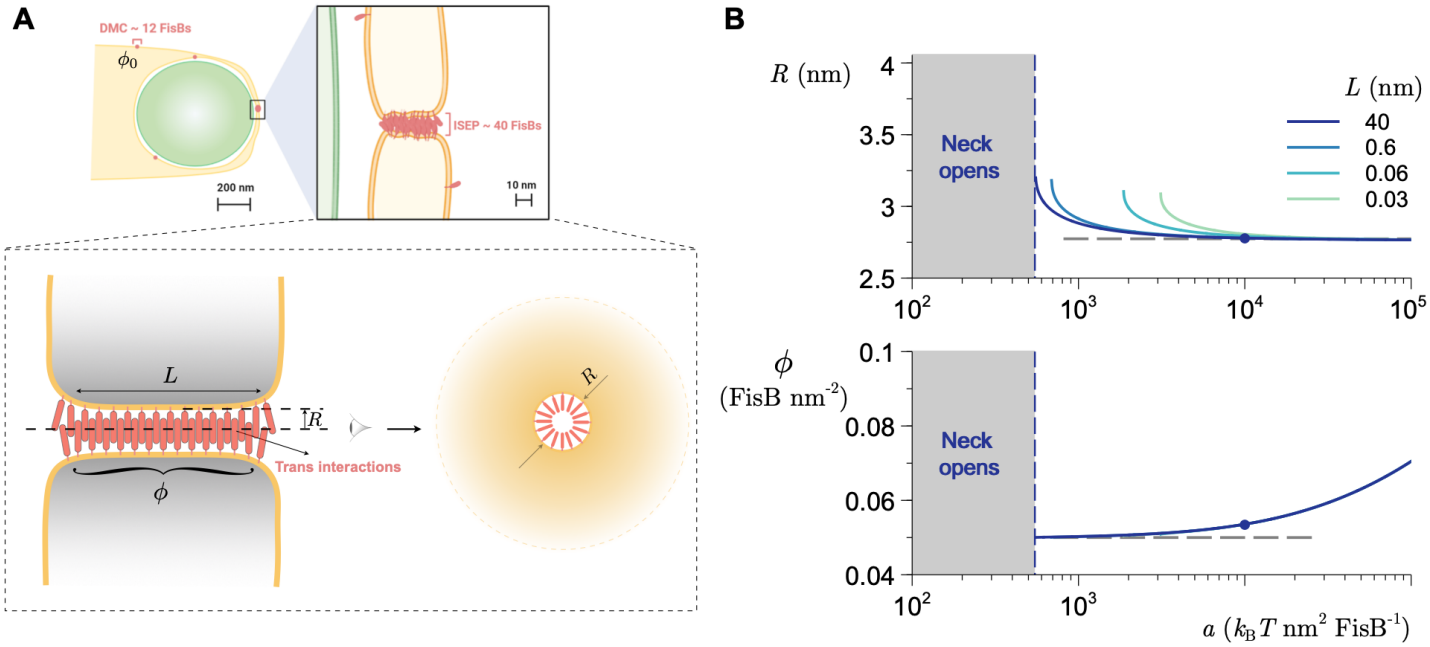
A
DMC ~ 12 FisBs
ϕ_0
200 nm
ISEP ~ 40 FisBs
10 nm
L
R
Trans interactions
ϕ
R
B
R (nm)
4
3.5
3
2.5
Neck opens
L (nm)
40
0.6
0.06
0.03
10^2
10^3
10^4
10^5
ϕ (FisB nm^{-2})
0.1
0.08
0.06
0.04
Neck opens
10^2
10^3
a ($k_B T$ nm^2 FisB^{-1})

FIGURE 9